Accepted Manuscript

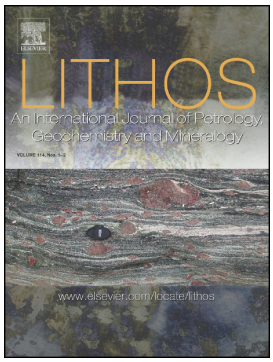

Contrasting Accessory Mineral behavior in minimum-temperature melts: empirical constraints from the Himalayan Metamorphic Core

John M. Cottle, Kyle P. Larson, Chris Yakymchuk

PII: S0024-4937(18)30160-9
DOI: doi:10.1016/j.lithos.2018.05.003
Reference: LITHOS 4649

To appear in:

Received date: 28 February 2018
Accepted date: 5 May 2018

Please cite this article as: John M. Cottle, Kyle P. Larson, Chris Yakymchuk , Contrasting Accessory Mineral behavior in minimum-temperature melts: empirical constraints from the Himalayan Metamorphic Core. The address for the corresponding author was captured as affiliation for all authors. Please check if appropriate. Lithos(2018), doi:10.1016/j.lithos.2018.05.003

Contrasting Accessory Mineral behavior in minimum-temperature melts: empirical constraints from the Himalayan Metamorphic Core

John M. Cottle[1*], Kyle P. Larson[2], Chris Yakymchuk[3]

[1]*Department of Earth Science, University of California, Santa Barbara, California 93106-9630, USA*

cottle@geol.ucsb.edu

[2]*Earth and Environmental Sciences, IKBSAS, University of British Columbia Okanagan, Kelowna, BC V1V 1V7, Canada*

[3]*Earth and Environmental Sciences, University of Waterloo, Waterloo, Ontario N2L 3G1, Canada*

**corresponding author*

1. Abstract

Medium-grained leucogranite in the Tama Kosi region of the Nepalese Himalayan Metamorphic Core yields a relatively narrow range of monazite $^{208}Pb/^{232}Th$ dates with a dominant population at ~ 21.0 Ma inferred to represent crystallization of an early plutonic phase. In contrast, the pegmatitic portion of the same intrusive complex, that cross-cuts the medium-grained leucogranite, contains zircon, monazite and xenotime that each display near-identical age spectra, recording semi-continuous (re-)crystallization from 27.5 Ma to 21.0 Ma, followed by a ~2 m.y. hiatus then further (re-)crystallization between 19.4 and 18.6 Ma. The 'gap' in pegmatite dates corresponds well to the crystallization age of the older leucogranite, whereas the end of accessory phase growth in the pegmatite coincides with the onset of regional-scale cooling. Detailed textural, trace element and thermochronologic data indicate that the range of zircon, monazite and xenotime dates recorded in the pegmatite reflect inherited components that underwent semi-continuous (re-)crystallization during metamorphism and/or anatexis in the source region(s), whereas dates younger than the hiatus indicate accessory phase recrystallization, related to both fluid influx and a concomitant increase in temperature. In contrast, the lack of an inherited component(s) in the medium-grained leucogranite phase is inferred to be a result of complete dissolution during partial melting. A model is proposed in which influx of heat and H_2O-rich fluids associated with early leucogranite emplacement temporarily delayed zircon and monazite and xenotime crystallization, respectively. These data highlight the importance of measuring spatially resolved dates, trace elements and textural patterns from multiple accessory minerals combined with model constraints to better understand the often-complex crystallization history of anatectic melts in collisional orogens.

Keywords: monazite, xenotime, zircon, recrystallization, Himalaya, leucogranite

2. Introduction

Within collisional orogens, investigation of crustally derived, or anatectic, granites (sensu lato) can reveal much about the thermal and rheological history of the system. The crystallization ages of such bodies, as determined by radioisotope geochronology, have been widely used as a tool to directly date both the timing and duration of igneous processes such as formation, mobilization, transport, differentiation and emplacement of melt into the mid-crust (e.g., Searle et al., 2009; Lederer et al., 2013; Weinberg, 2016), a means to bracket, or at least indirectly infer, the absolute timing and duration of fabric development and movement on shear zones and faults via cross-cutting relationships (e.g., Murphy and Harrison, 1999) and as a proxy for timing and duration of high-grade metamorphism (e.g. Rubatto et al., 2001).

The majority of geochronologic studies of anatectic granites rely on U-Th/Pb isotope ratio measurements of accessory minerals such as zircon, monazite and xenotime. A key goal in such studies is to determine the major factors that lead to the growth and/or dissolution of these minerals before, during, and potentially after, igneous or metamorphic crystallization, so that the isotopic dates can be linked to the bulk rock history. Using this information, isotopic dates can then be assigned a geologically meaningful age. In pursuit of this goal, the relative roles of pressure, temperature, and fluid composition (P-T-X) in controlling accessory phase precipitation, growth and dissolution have been extensively investigated via both empirical (e.g., Foster et al., 2004) and experimental (e.g., Rapp et al., 1987; Seydoux-Guillaume et al., 2002) approaches.

Although zircon is arguably the most commonly used igneous U/Pb geochronometer, its application to dating crystallization of low-temperature crustal melts is problematic. Because

crustal anatexis typically occurs at, or close to minimum 'wet-solidus' temperatures (e.g. Harris and Massey 1984), and zircon solubility is strongly sensitive to temperature (e.g., Watson and Harrison, 1983; Boehnke et al., 2013), there is typically minimal zircon dissolution in strongly peraluminous melts leading to the ubiquitous presence of inherited zircon and only small amounts of newly grown zircon, typically forming micron-scale rims surrounding inherited cores. In addition, zircons in anatectic granites often contain 1000's of ppm U, which may cause radiation damage, metamictization and open system behavior of Pb (e.g., Nasdala et al., 2001) as well as complicating analysis my microanalytical techniques (e.g., Parrish, 2009).

Because of the often-complex nature of zircon age systematics in anatectic granites and the analytical challenges associated with measuring such thin rims, many workers have instead employed monazite as the chronometer of choice. Monazite has several useful characteristics that make it an ideal chronometer in such systems: It contains high concentrations of parent actinide (usually several weight % Th, and 100's to several 1000 of ppm U); it typically contains small amounts of common lead; is not thought to undergo thermally mediated volume diffusion of lead at typical crustal conditions (Parrish, 1990); it incorporates a variety of geologically useful trace elements (principally Y + REE, but also Sr, Ca); is reactive across a range of P-T-X conditions and can potentially record multiple episodes of dissolution and re-precipitation in a single crystal (e.g., Williams et al., 2007).

Despite the widespread use of monazite as a geochronometer in minimum-temperature melts, key questions remain including - how do dates obtained from monazite compare to other accessory phases such as zircon or xenotime in terms of recording specific geologic processes given that their (re-)crystallization histories may be differentially affected by changes in P-T-X? Why do some anatectic granites contain either whole monazite crystals and/or relict crystal

portions that are demonstrably older than the crystallization age (e.g., Copeland et al., 1988), yet other geochemically similar melts in the same area apparently do not record such complexity (e.g., Lederer et al., 2013; Cottle et al., 2015)? If inherited components can be identified, what if any, is their geologic and/or geochemical significance?

To address these questions, this study examines anatectic leucogranites from a geologically well-constrained portion of the Himalayan metamorphic core, the Tama Kosi region of Nepal (Fig. 1). These samples offer two useful insights. Firstly, the rocks contain multiple accessory minerals common in crustal granites (i.e. zircon, monazite and xenotime). Secondly, the exposure and geologic context is sufficiently well understood that it is also possible to confidently compare data from the granites to that of the inferred restitic portion of the system. In this contribution, these rocks are subjected to detailed textural, geochemical and petrochronologic analysis in order to establish the relative behavior of each of the accessory phases, identify, and develop a model that offers an explanation for the differences observed among genetically related melts and their source region.

3. Geologic Background

Initial geologic characterization of the Tama Kosi valley region of east-central Nepal focused on the lower reaches of the drainage (Fig. 1; Ishida, 1969; Schelling, 1992). The geology of the upper Tama Kosi was first investigated at a reconnaissance scale by Larson (2012) who noted a significant amount of leucogranitic anatexite. Evidence of melting is not restricted to a single form, but rather manifested as a series of different bodies varying from large-scale (~20 km^2 in outcrop pattern) plutons (Fig. 1) to outcrop scale migmatite (Fig. 2). Dykes and sills related to

plutonic bodies intrude the country rock and crosscut the regional foliation (Larson, 2012) making the determination of its age important to constrain regional deformation and associated metamorphism.

An ~6 x 5 km plutonic body is mapped at the head of the Tama Kosi valley (Figs. 1, 2). Two main phases are recognized within it. Based on field relationships, the oldest phase is a medium to coarsely crystalline quartz + feldspar + biotite + muscovite leucogranite (Figure 3; Larson, 2012). This phase is crosscut by a coarse to pegmatitic feldspar + quartz + muscovite leucogranite (Fig. 2B, C, Fig 3A). In the field area, clear cross-cutting relationships exist (e.g., Fig. 2A, B) that indicate that the medium to coarse-grained phase (sample TK122, Fig 3B) is demonstrably older than the pegmatitic phase (TK111B).

Limited geochronologic data from the Tama Kosi region indicate that synkinematic metamorphism took place at the lowest structural positions in the Himalayan Metamorphic Core between 10 and 8 Ma (sample TK45 Fig. 1) while protracted metamorphism in the middle portion of the HMC occurred between 22 and 18 Ma with evidence for in-situ partial melting and melt crystallization at 15-14 Ma (TK21 and TK27, Fig. 1, Larson et al., 2013). The only constraints from a similar structural position to the samples studied here comes from ~20 km to the east where a sillimanite-grade metamorphic rock contains 24 – 21 Ma monazite cores inferred to record near-peak metamorphic conditions and 19 – 16 Ma rims consistent with (re-)crystallization during melting and/or retrograde metamorphism (TK139, Fig. 1, Larson and Cottle, 2014).

4. Methods

4.1 Geochronology Methods

With the exception of TK116 that was analyzed directly in thin section, accessory minerals were liberated from ~2 kg samples by standard crushing, hydrodynamic, heavy liquid and isodynamic magnetic separation techniques. At least fifty crystals of each mineral were picked by hand under a binocular microscope, mounted in epoxy resin, and polished finishing with 0.25 μm diamond. Backscatter-electron (BSE), cathodoluminescence (CL) and WDS x-ray images were collected using scanning electron microscopy (SEM), and Electron Probe MircoAnalyzer (EPMA, monazite and xenotime only) to provide textural context for LASS-ICPMS spot analysis placement.

Minerals were analyzed using the Laser Ablation Split Stream setup housed at the University of California, Santa Barbara. The LASS-ICP-MS system combines a Photon Machines 193 nm ArF Excimer laser and Hel-Ex ablation cell with a Nu Instruments HR Plasma high-resolution multi-collector MC-ICP-MS for collecting U-Th/Pb data and an Agilent 7700S quadrupole Q-ICP-MS for collecting major and trace element data. Methods used in this study follow those outlined by Kylander-Clark *et al*. (2013), with modifications presented by McKinney et al., (2015).

Zircon was ablated using a 15μm diameter spot at 4Hz repetition rate for 100 shots at a laser fluence of 1.5 J/cm^2, resulting in craters that are ~7 μm deep. Monazite and xenotime were using a 8μm diameter spot at 3Hz repetition rate for 100 shots at a laser fluence of 1.5 J/cm^2, resulting in craters that are ~5 μm deep.

Zircon U-Th/Pb and trace element data was normalized to '91500' (1062.4 Ma $^{206}Pb/^{238}U$ ID-TIMS age; Wiedenbeck et al., 1995) and 'GJ-1' (using trace element values of Liu et al., 2010) reference zircons respectively, while monazite and xenotime U-Th/Pb and trace element data were normalized to '44069' (424 Ma Pb/U ID-TIMS age, Aleinikoff et al., 2006) and

'Bananeira' (508.9 Ma Pb/U LA-ICP-MS age and trace element values of Kylander-Clark et al., 2013) reference monazites, respectively.

Eleven analyses of SL-2 zircon (563 ± 5 Ma, Gehrels et al., 2008) treated as an unknown in order to assess accuracy and precision and run throughout the analytical session yield a weighted mean $^{206}Pb/^{238}U$ date of 571 ± 4 Ma, MSWD = 1.3. Thirteen analyses of Bananeira monazite yield a weighted mean $^{206}Pb/^{238}U$ date of 511 ± 3 Ma, MSWD = 1.3. Sixteen analyses of monazite FC-1 (55.6 Ma ID-TIMS age, Horstwood et al., 2003) yield a weighted mean $^{206}Pb/^{238}U$ date of 56.0 ± 0.3 Ma, MSWD = 0.6, and a weighted mean $^{208}Pb/^{232}Th$ date of 55.1 ± 0.4 Ma, MSWD = 1.4. Based on the long-term reproducibility of multiple secondary reference minerals, trace element concentrations are accurate to 3-5% (2σ).

A ^{207}Pb-based correction was applied to zircon and xenotime using a common lead composition derived from the single stage model of Stacey and Kramers (1975) at the inferred crystallization age. The uncertainty on the ^{207}Pb corrected age incorporates uncertainties on the measured $^{206}Pb/^{238}U$ and $^{207}Pb/^{206}Pb$ ratios as well as a 1% uncertainty on the assumed common lead composition.

Monazite incorporates significant amounts of ^{230}Th into its structure during crystallization, leading to formation of 'excess' ^{206}Pb and resulting in disequilibrium in the $^{238}U \rightarrow {}^{206}Pb$ decay chain (Schärer, 1984). In young (Cenozoic) monazites this results in apparent $^{206}Pb/^{238}U$ dates that are older than measured $^{207}Pb/^{235}U$ and $^{208}Pb/^{232}Th$ dates (neither of which are affected by this issue) by as much as 50% (e.g. Cottle et al., 2009). In addition, because of their young age, such monazites typically contain a relatively low amount of radiogenic ^{207}Pb, resulting in $^{207}Pb/^{235}U$ dates that are less precise than $^{206}Pb/^{238}U$ and $^{208}Pb/^{232}Th$ dates. Because monazite

contains weight % levels of ^{232}Th and therefore significant ^{208}Pb we therefore take the LA-MC-ICPMS ^{208}Pb/^{232}Th dates as the as the best estimate of the monazite crystallization age.

U-Th/Pb data were plotted using the Redux v.3.0.4 (Bowring et al., 2011). The complete U-Th/Pb data are presented in Table DR 1.

4.2 Accessory Phase Thermometry

Ti-in-zircon apparent temperatures were calculated using the calibration of Ferry and Watson (2007). TiO_2 activity was assumed to be 0.8 ± 0.2, based on the apparent lack of primary rutile, and SiO_2 activity to be 1, based on the presence of quartz. Uncertainty in elemental concentration (2 S.E.), TiO_2 activity, and SiO_2 activity are propagated into the reported temperature uncertainties. Y-in-mnz apparent temperatures were calculated using the calibration of Gratz and Heinrich (1997) assuming a pressure of 4 kbar. Uncertainty in elemental concentration (2 S.E.) is propagated into the reported temperature uncertainties.

4.3 Geochemistry Methods

Whole-rock major elements were measured via X-ray fluorescence (XRF) spectrometry at Pomona College at Pomona, following methods outlined in Johnson *et al*., (1999). Glass beads were produced by powdering samples in a tungsten carbide (WC) ring mill, mixing with lithium tetraborate flux in a 2:1 ratio, and doubly fused in graphite crucibles at 1000 ^{0}C for 40 minutes. Whole-rock trace elements were measured by LA-Q-ICP-MS at UCSB on small chips of the same glass beads used for XRF, following methods outlined in Poletti et al., (2016).

5. Results

5.1 Accessory Phase Textures

Zircon from the pegmatitic phase of the intrusive complex, TK111B, contains patchy-zoned or homogeneous cores mantled by a domain(s) with variably preserved oscillatory zoning (Fig. 4A). Monazite is typically either sector-zoned or oscillatory-zoned with occasional evidence for patchy-zoned relict cores (Fig. 4B) while xenotime contains poikloblastic and/or patchy zoned cores (inclusions are typically either UO_2 [bright patches in Figure 4C], feldspar or quartz), surrounded by distinct oscillatory-zoned rims (Fig. 4C). Monazite from the coarse-grained leucogranite, TK122, contains patchy zoned cores surrounded by an oscillatory-zoned rim that makes up the outer half to three quarters of the crystal (Fig. 4D). Specimen TK116, a restitic layer near the margin of the main plutonic body, contains small (<80 μm diameter) monazite with broadly concentric zoning in which the REE, Y and U (Fig. 3E) increase toward the rim. Xenotime shows a similar pattern, with the exception of U, which decreases from core to rim (Fig. 4F)

5.2 Geochronology Data

Zircon, monazite and xenotime from the pegmatitic phase, TK111B, present a complex distribution of dates. All three minerals yield a similar, semi-continuous, range of dates from ~27.5 Ma to ~18.6 Ma, with each mineral showing a distinct absence of dates at ~20.3 Ma (Fig. 5A, B, C and 6). Accessory mineral dates younger than ~20.3 Ma overlap; Zircon records a date of 19.3 ± 0.3 Ma, MSWD = 2.0 (n=5), monazite yielding a single population at 19.1 ± 0.1 Ma (MSWD = 1.0, 1 out of 18 rejected), and xenotime recording two distinct dates of 19.4 ± 0.3 Ma, MSWD = 0.5 (n=4) and 18.6 ± 0.2 Ma, MSWD = 0.2 (n=4). In summary, zircon, monazite and

xenotime are inferred to have (re-)crystallized from 27.5 Ma to 21 Ma, followed by a 1.3 – 2.2 m.y. hiatus and further (re-)crystallization between 19.5 and 18.6 Ma.

Monazite from the restitic phase, TK116, yield a spread in dates similar to specimen TK111B, with the majority of analyses falling between 23 and 25 Ma, with dates as old as c. 32 Ma (Fig. 5E, F). Although fewer in number, xenotime analyses form a comparable spread to the monazite dates. In contrast to the other samples in this study, there are no monazite and xenotime dates younger than ~20.5 Ma.

The medium-to coarse phase, specimen TK122, has a relatively straightforward distribution of dates compared to the complex systematics observed in the pegmatitic and restitic phases. Thirty out of 48 analyses yield a distinct population at 21.0 ± 0.1 Ma, MSWD = 1.5 (Fig. 5D and 6), which is taken as the best estimate of the crystallization age of the coarse-grained phase of the intrusive complex.

5.3 Interpretation of Accessory Phase Geochemistry

In sample TK111B, the total rare earth element (REE) abundance in monazite and xenotime remains approximately constant from 27 Ma to 18.5 Ma, whereas over the same time period, zircon shows half an order of magnitude decrease (Fig. 7A), consistent with the partitioning of REE into monazite and xenotime relative to zircon. An increase in both monazite and xenotime Eu/Eu* indicates decreasing feldspar abundance or fractionation from 27 to 21 Ma (Fig. 7B). At 19 Ma the Eu anomaly decreases to a similar value as at 27 Ma (Fig. 7B) compatible with either minor feldspar dissolution or influx of melt at ~ 19 Ma. Zircon Eu/Eu* is highly variable, but generally follows the same trend as monazite and xenotime. The average zircon Th/U ratio

decreases fourfold from 0.015 at ~27 Ma, to 0.004 at ~21 Ma (Fig. 7C). Monazite Th/U also decreases, from 4.05 at ~27 Ma to ~2.10 at 21 Ma, and xenotime decreases from 0.14 at ~27 Ma to 0.055 at ~21 Ma (Fig. 7C). The marked change in Th/U ratio in monazite, xenotime and zircon through time is largely a result of decreasing U and is indicative of either gradual depletion in U by progressive sequestration into earlier formed accessory minerals with low Th/U or a change in oxidation state (U^{4+} is converted to the less compatible U^{5+} and U^{6+}). Gradual changes in the Sm/La and Gd/Yb ratios (Fig. 7D-F), proxies for the LREE and HREE slopes respectively, indicate progressive co-crystallization of monazite and xenotime and zircon from 27 – 21 Ma. Matching step functions in the Sm/La and Gd/Yb ratios of xenotime at 24 – 22.5 Ma (Fig. 7E) potentially reflect an interval of decreased monazite and/or apatite modal abundance.

Similar to TK111B, the total REE abundance forms a decreasing trend with time in TK116 monazite and xenotime (Fig. 8A), indicating progressive crystallization and an increase in modal abundance of REE-bearing phases. The lower and more variable Eu/Eu* in TK122 monazite may reflect significant plagioclase fractionation, consistent with the greater modal abundance of feldspar in this rock compared to either TK111B or TK116 (Fig. 8B). The Eu anomaly in monazite and xenotime from TK116 show opposite trends with monazite increasing through time and xenotime decreasing through time (Fig. 7B). The monazite Th/U ratio in TK122 is consistent at 5.7 (c.f. whole rock value of 0.18) similar to monazite in both TK111B and TK116 (Fig. 8C). In contrast to TK111B, in TK116, from 28 – 21 Ma, xenotime Th/U increases, while monazite Th/U decreases with near-constant U, and decreasing Th. This trend could reflect increased fractionation of monazite through time. TK122 monazite Sm/La and Gd/Yb ratios are significantly more variable than any of the other samples in this study (Fig. 8D, E). Sm/La and

Gd/Yb ratios in TK116 monazite and xenotime are consistent with progressive co-fractionation of these phases through time (Fig. 8D, E).

Geochronology and trace element data indicate that similar, protracted histories of accessory phase crystallization are recorded in TK111B and TK116. Making the assumption that equilibrium was achieved and maintained throughout the rock history, it is possible to calculate equilibrium partition co-efficients (K_D) through time for mineral pairs. To obtain representative data, trace element concentrations were averaged over 1 m.y. intervals, and used to compute K_D values. An illustrative plot of Yttrium K_D is shown in Figure 9 and indicates consistent K_D for mineral pairs from 27 – 21 Ma. The distinct change in Yttrium K_D observed in TK111B at ~25 Ma is potentially explained by an increasing in the modal abundance of a Y-bearing mineral. Plots of other elements and element ratios display similar trends (not shown).

5.4 Accessory Phase Thermometry

Ti-in-zircon temperatures for zircon in TK111B and Y-in-monazite thermometry for TK111B and TK116 were calculated using the calibrations of Ferry and Watson (2007) and Gratz and Heinrich, (1997) respectively (Fig. 10). Because the intra-sample ranges in monazite and xenotime dates overlap in both TK111B and TK116, it is reasonable to assume that within each of these specimens, monazite and xenotime were potentially in equilibrium throughout the history of the rocks. It is therefore feasible to calculate apparent temperatures for all of the spot analyses. Since there are no pressure constraints for this rock, Ti- and Y-temperatures were calculated at 4 kbar (consistent with regional PT constraints during melt formation, e.g., Larson et al., 2013). Changing the estimated pressure by ± 0.5 kbar does not change the calculated

temperatures appreciably; the uncertainty on the LA-ICPMS Ti and Y concentration measurement is the greatest contributor to the uncertainty on the measured temperatures, and this is propagated through to the final uncertainty on the temperature estimate. No Y-in-monazite temperatures were calculated for TK122 as no xenotime was observed in that rock.

For TK111B, there is no apparent correlation between age and either Ti- or Y-temperature, with the zircon and monazite yielding weighted mean temperatures of 580 ± 20 C (2 S.E.) and 605 ± 50 C respectively. In contrast to TK111B, in sample TK116 there is a moderately good correlation between temperature and age. Between 27 and 21.5 Ma, the mean Y-in-monazite temperature increases by c. 25^{o}C / m.y (R^2 = 0.4 on a linear fit) from 500^{o}C at 27 Ma, to 650^{o}C at 21 Ma (Fig. 10).

Apparent temperatures calculated for <20 Ma monazite in TK116 range from from 600 – 800^{o}C. The <700^{o}C data are consistent with the 'older' temperature estimates, while those > 700^{o}C appear not to fit the overall pattern (Fig. 10). Inspection of the raw data indicates that analytical artifacts, including the presence of Y-bearing inclusions can be ruled out. Given that such high temperatures are not recorded by zircon in the same sample, these anomalously high values are inferred not be geologically meaningful and are instead interpreted to represent post-20 Ma disequilibrium in Y-partitioning between monazite and xenotime.

5.5 Model Constraints

Zircon solubility in melt is primarily a function of temperature and to a lesser extent the bulk composition variable 'M', which is equal to the molar ratio [(Na+K+2Ca)/(Al x Si)] of the melt (e.g. Watson and Harrison, 1983). The values of M for samples TK111B and TK122 are 1.06

and 1.11, respectively. Using the experimentally derived zircon solubility expression from Boehnke et al. (2013) with the bulk rock values of M and the bulk concentrations of Zr, this equates to zircon saturation temperatures of 675 ± 10°C and 685 ± 10°C, respectively (Fig. 11A). Similarly, LREE saturation of the melt with respect to monazite (and therefore the point of monazite crystallization) is a function of temperature and the melt H_2O content and, to a lesser extent, pressure and the molar ratio of the LREE to the sum of all cations (e.g. U, Th, REE) in monazite (Stepanov et al. 2012). Using the monazite solubility expression of Stepanov et al. (2012) coupled with the bulk rock LREE concentrations obtained by ICP-MS and the average molar ratios of LREE in monazite from each sample, saturation temperatures were calculated at 4 kbar over a range of H_2O compositions (Fig. 11B). For 5 wt.% H_2O in melt, which similar to experimentally derived estimates for water in Himalayan leucogranites (e.g., Scalliet et al., 1996), the calculated monazite saturation temperatures of TK122 and TK111B are 705 ± 45°C and 620 ± 45°C, respectively (Fig. 10B). Based on these results, both zircon and monazite are expected to crystallize from anatectic melt at temperatures at or just above the wet granite solidus.

6. Discussion

6.1 Protracted (re-)crystallization in source region of pegmatite

The 27.5 – 21 Ma range of dates preserved in TK111B monazite, xenotime and zircon likely reflects one or more of the following processes: 1) protracted igneous crystallization and/or fluid-induced recrystallization; 2) inheritance; 3) mechanical mixing or; 4) Pb-loss. Radiogenic Pb-loss can be ruled out because the nominal closure temperature for thermally-mediated volume

diffusion of Pb in these minerals is >900 ^{o}C, (e.g. Schmitz and Bowring, 2003; Cherniak and Watson, 2001; Cherniak et al., 2004), which is at least 250 ^{o}C above peak temperatures achieved in this part of the Himalayan mid crust (c. 750^{o}C, e.g. Larson et al, 2013). Likewise, mechanical mixing such that the analytical spot overlapped multiple domains in either the X-Y and/or Z direction can be ruled out on the basis that binary mixing calculations cannot reproduce the observed trends in trace elements. Careful evaluation of time- and depth-dependent isotopic signals reveals no variability in age with depth of individual sports and all included analyses were confirmed to be located entirely within a single domain through detailed comparison of x-ray maps superimposed on post-ablation optical images.

Deciphering whether the 27.5–21 Ma age range in TK111B represents protracted igneous (re-)crystallization or inheritance from the melt source region is more difficult. We prefer the latter interpretation of inheritance from the source for two reasons: 1) TK111B cross-cuts the main leucogranite phase TK122 and is therefore younger. If the spread in data observed in TK111B is related to protracted thermal- or fluid-mediated (re-)crystallization after emplacement of the pegmatite, it would be reasonable to expect a similar disturbance to other rocks at the same location, in particular the older rock, TK122. No such spread is seen in TK122, and implies that the older components in TK111B pre-date crystallization of the pegmatite itself. 2) The pattern of ages older than 21 Ma and the calculated Y-in-monazite temperature observed in TK111B are very similar to those in restite sample TK116, indicating a shared thermal and temporal history between a known source for melt (i.e. TK116) and a product of melting (TK111B). We therefore conclude that all of the accessory phases older than 21 Ma in TK111B are inherited from the source region and do not reflect the igneous history of the pegmatite itself. This implies that only the youngest 19.4 and 18.6 Ma ages in the pegmatite record the final igneous crystallization of

this body. Equally, the Y-in-monazite and Ti-in-zircon temperatures in TK111B and TK116 indicate that near-isothermal conditions of ~ 650-700 ^{o}C were maintained in the source region of the Himalayan metamorphic core for at least 9 m.y. from 30 – 21 Ma.

6.2 Origin of 21 – 19.5 Ma 'gap' in data

The 21 – 19.5 Ma 'gaps' in TK111B zircon, monazite and xenotime ages are similar in absolute time and duration to each other. In addition, the 19.4 and 18.6 Ma ages younger than the 'gap', are also strikingly similar (Fig. 5 and 6). Together these patterns suggest that the process(es) responsible for shutting off accessory phase (re-)crystallization during this time period had the same effect on all of the minerals. The 'gap' in dates in the pegmatite phase is also somewhat unusual, especially given the observation that prior to this there was ~9 m.y. of semi-continuous zircon, monazite and xenotime co-(re-)crystallizing in the general source region, i.e. TK116 and the inherited component of TK111B. Based on geochronology data, the gap in dates observed in TK111B corresponds well to emplacement and crystallization of the cross-cutting monazite-bearing coarse-grained leucogranite (TK122; 21.1 – 19.8 Ma) (Fig. 5 and 6). While there is a good temporal correlation between these two observations, the geochronology data do not provide a mechanistic reason for the existence of the gap in dates between those inherited from the source (27 – 21 Ma), and those that reflect final igneous crystallization (19.4 – 18.6 Ma). To gain further insight into the origin of the 'gap' in data in TK111B, it is necessary to combine the geochronology and accessory phase trace element data with experimentally derived model constraints.

Zirconium and LREE- saturation calculations indicate that in these rocks, zircon crystallization is primarily a function of temperature (lower temperature equates to greater zircon crystallization), whereas monazite (and xenotime?) crystallization is dominantly controlled by the concentration of H_2O in the melt (lower H_2O equates to greater monazite crystallization). Any model that seeks to clarify the origin of the 'gap' in ages must explain not only zircon, but also monazite and xenotime, and therefore requires a process that perturbs both the temperature and H_2O content of the source region for TK111B.

One viable explanation for the break in age data consistent with both the geochronology data and the model constraints is that the gap is fundamentally driven by thermal and chemical effects of the emplacement of a generation of melt(s), similar to TK122, into the source region of TK111B. A schematic model for the melt history is shown in Figure 12. Initial, protracted crystallization of monazite, xenotime and zircon in the (future) source region of TK111B (Fig. 12A) is followed by emplacement of TK122 generation melts (Fig. 12B), and finally melt extraction to form TK111B. Emplacement of TK122 generation melts would result in both an increase in temperature of sufficient magnitude that delayed further zircon crystallization. Emplacement of these melts was also likely accompanied by in an influx of H_2O exsolved from the crystallizing magma. The influx of H_2O effectively delayed further monazite and xenotime growth, and may have even promoted dissolution. The origin of the 'gap' in ages in TK111B is thus a combined effect of heat and H_2O influx driven by emplacement of leucogranite melt (Fig. 12B). The increase in temperature and influx of H_2O may also have been enough to initiate melting in the source region for TK111B, producing a slightly younger generation of coarse-grained and/or pegmatitic bodies. Emplacement, cooling and crystallization of these bodies, like TK111B, promoted further accessory phase (re-)crystallization, produced ages younger than the

'gap' and are the only portion of the minerals to record the igneous crystallization of the melt in which they reside (Fig. 12C).

6.3 Variable inheritance in Tama Kosi leucogranites

In the Tama Kosi region, there is a clear difference in accessory phase inheritance pattern between the pegmatitic phase (e.g., TK111B) that records ages up to 10 m.y. older than the timing of final crystallization, whereas other, broadly contemporaneous, leucogranites (e.g., TK122) from the same outcrops contain no resolvable inheritance, at the percent level of precision (i.e. 200 ka) obtainable by LA-ICP-MS. A similar observation has been made elsewhere in the Himalayan core, where different inheritance patterns are observed in both different age leucogranites at the same outcrop as well as contemporaneous leucogranites from different outcrops in the same area (e.g., Harrison et al., 1995; Viskupic and Hodges, 2001; Viskupic et al., 2005; Lederer et al., 2013; Cottle et al., 2015). There are several processes that may lead to inheritance, including: wall-rock assimilation, magma mixing; and incomplete accessory phase dissolution during melting. Himalayan leucogranites are dominantly minimum temperature melts (Harris and Massey, 1984), and therefore have limited thermal ability to assimilate wall-rock (including accessory minerals) without immediate cooling and crystallization. Similarly, it is possible that physical mixing of different melts may result in inheritance, but because of the low temperature and high viscosity of Himalayan leucogranite melts, the time-scales available for magma mixing are very short. Thus, magma mixing can only explain inherited components relatively close to the final crystallization age, but not inheritance several m.y. older. It therefore seems mostly likely that variable inheritance patterns are dominantly a result of the degree to which monazite and other accessory phases present in the source are dissolved during melting. As previously discussed, melts at higher temperature, and in

the presence of greater water content result in greater dissolution of accessory phases. Thus, Himalayan leucogranites with greater evidence of inheritance are inferred to be a result of melting at lower temperature (in the case of zircon) and/or with greater water content (in the case of monazite and xenotime).

7. Conclusions

Accessory zircon, monazite and xenotime from pegmatites in the Himalayan metamorphic core of the Tama Kosi region, Nepal display complex age spectra with semi-continuous (re-)crystallization over an ~8 m.y. time period followed by a ~2 m.y. hiatus then further (re-)crystallization. The protracted record of ages preserved in the pegmatite is inferred to be a result of both inheritance from the source region (ages >21 Ma), and subsequent igneous crystallization (19.4 – 18.6 Ma ages). The hiatus in accessory phase (re-)crystallization is likely a result of emplacement of ~21 Ma leucogranites into the vicinity of the source region for the pegmatite, accompanied by significant influx of heat and H_2O. Accumulation of heat halted zircon (re-)crystallization while the addition H_2O had a similar affect on monazite and xenotime. It is the combined effect of increased temperature and H_2O that results in a 'gap' in recorded ages and therefore reflects fundamental controls on the preservation of specific geologic events in low temperature igneous systems. This study also reinforces that to understand the complex crystallization history of anatectic melts it is necessary to combine textural data, detailed petrochronology and model constraints.

8. Acknowledgements

This study was supported by NSF grant EAR-1119380 to J. Cottle and NSERC Discovery and Canadian Foundation for Innovation grants to K. Larson. Jade Star Lackey, Andrew Kylander-Clark and Gareth Seward are thanked for their assistance with XRF, LA-ICP-MS and EPMA data collection, respectively. We thank the reviewers for their helpful suggestions that improved this manuscript.

9. References

Boehnke, P., Watson, E.B., Trail, D., Harrison, T.M., Schmitt, A.K., 2013. Zircon saturation re-revisited. Chem. Geol. 351, 324–334. https://doi.org/10.1016/j.chemgeo.2013.05.028

Bowring, J.F., McLean, N.M., Bowring, S.A., 2011. Engineering cyber infrastructure for U-Pb geochronology: Tripoli and U-Pb_Redux. Geochemistry, Geophys. Geosystems 12, n/a-n/a. https://doi.org/10.1029/2010GC003479

Cherniak, D., Watson, E.., 2001. Pb diffusion in zircon. Chem. Geol. 172, 5–24. https://doi.org/10.1016/S0009-2541(00)00233-3

Cherniak, D., Watson, E.B., Grove, M., Harrison, T.M., 2004. Pb diffusion in monazite: a combined RBS/SIMS study. Geochim. Cosmochim. Acta 68, 829–840. https://doi.org/10.1016/J.GCA.2003.07.012

Copeland, P., Parrish, R.R., Harrison, T.M., 1988. Identification of inherited radiogenic Pb in monazite and its implications for U–Pb systematics. Nature 333, 760–763. https://doi.org/10.1038/333760a0

Cottle, J.M., Searle, M.P., Jessup, M.J., Crowley, J.L., Law, R.D., 2015. Rongbuk re-visited: Geochronology of leucogranites in the footwall of the South Tibetan Detachment System, Everest Region, Southern Tibet. Lithos 227, 94–106. https://doi.org/10.1016/j.lithos.2015.03.019

Ferry, J.M., Watson, E.B., 2007. New thermodynamic models and revised calibrations for the Ti-in-zircon and Zr-in-rutile thermometers. Contrib. to Mineral. Petrol. 154, 429–437. https://doi.org/10.1007/s00410-007-0201-0

Foster, G., Parrish, R.R., Horstwood, M.S.A., Chenery, S., Pyle, J., Gibson, H.D., 2004. The generation of prograde P-T-t points and paths; a textural, compositional, and chronological study of metamorphic monazite. Earth Planet. Sci. Lett. 228, 125–142. https://doi.org/10.1016/j.epsl.2004.09.024

Gratz, R., Heinrich, W., 1997. Monazite-xenotime thermobarometry: Experimental calibration of the miscibility gap in the binary system CePO4-YPO4. Am. Mineral. 82, 772–780.

Harris, N., Massey, J., 1994. Decompression and anatexis of Himalayan metapelites. Tectonics 13, 1537–1546. https://doi.org/10.1029/94TC01611

Harrison, E.B.W. and T.M., 1983. Zircon saturation reviseted: temperature and composition effects in a variety of crustal magmas types. Planetarry Sci. Lett. 64, 295–304.

Harrison, T.M., McKeegan, K.D., LeFort, P., 1995. Detection of inherited monazite in the Manaslu leucogranite by $^{208}Pb/^{232}Th$ ion microprobe dating: Crystallization age and tectonic

implications. Earth Planet. Sci. Lett. 133, 271–282. https://doi.org/10.1016/0012-821X(95)00091-P

Ishida, T., 1969. Petrography and structure of the area between the Dudh Kosi and the Tamba Kosi, east Nepal. J. Geol. Soc. Japan 75, 115–125. https://doi.org/10.5575/geosoc.75.115

Johnson, D.M., Hooper, P.R., Conrey, R.M., 1999. XRF analysis of rocks and minerals for major and trace elements on a single low dilution Li-tetraborate fused bead. Adv. X-ray Anal. 41, 843–867.

Kylander-Clark, A.R.C., Hacker, B.R., Cottle, J.M., 2013. Laser-ablation split-stream ICP petrochronology. Chem. Geol. 345, 99–112. https://doi.org/10.1016/J.CHEMGEO.2013.02.019

Larson, K.P., 2012. The geology of the Tama Kosi and Rolwaling valley region, East-Central Nepal. Geosphere 8, 507–517. https://doi.org/10.1130/GES00711.1

Larson, K.P., Cottle, J.M., 2014. Midcrustal discontinuities and the assembly of the Himalayan midcrust. Tectonics 33, 718–740. https://doi.org/10.1002/2013TC003452

Larson, K.P., Gervais, F., Kellett, D.A., 2013. A P-T-t-D discontinuity in east-central Nepal: Implications for the evolution of the Himalayan mid-crust. Lithos 179, 275–292. https://doi.org/10.1016/j.lithos

Lederer, G.W., Cottle, J.M., Jessup, M.J., Langille, J.M., Ahmad, T., 2013. Timescales of partial melting in the Himalayan middle crust: insight from the Leo Pargil dome, northwest India. Contrib. to Mineral. Petrol. 166, 1415–1441. https://doi.org/10.1007/s00410-013-0935-9

McKinney, T.S., Cottle, J.M., Lederer, G.W., 2015. Evaluating rare earth element (REE) mineralization mechanisms in Proterozoic Gneiss, Music Valley, California. Bull. Geol. Soc. Am. 127, 1135–1152. https://doi.org/10.1130/B31165.1

Murphy, M.A., Mark Harrison, T., 1999. Relationship between leucogranites and the Qomolangma detachment in the Rongbuk Valley, south Tibet. Geology 27, 831. https://doi.org/10.1130/0091-7613(1999)027<0831:RBLATQ>2.3.CO;2

Nasdala, L., Wenzel, M., Vavra, G., Irmer, G., Wenzel, T., Kober, B., 2001. Metamictisation of natural zircon: accumulation versus thermal annealing of radioactivity-induced damage. Contrib. to Mineral. Petrol. 141, 125–144. https://doi.org/10.1007/s004100000235

Parrish, R.R., 1990. U–Pb dating of monazite and its application to geological problems. Can. J. Earth Sci. 27, 1431–1450. https://doi.org/10.1139/e90-152

Poletti, J.E., Cottle, J.M., Hagen-Peter, G.A., Lackey, J.S., 2016. Petrochronological constraints on the origin of the Mountain Pass ultrapotassic and carbonatite intrusive suite, California. J. Petrol. 57, 1555–1598. https://doi.org/10.1093/petrology/egw050

Rapp, R.P., Ryerson, F.J., Miller, C.F., 1987. Experimental evidence bearing on the stability of monazite during crustal anaatexis. Geophys. Res. Lett. 14, 307–310. https://doi.org/10.1029/GL014i003p00307

Rubatto, D., Williams, I.S., Buick, I.S., 2001. Zircon and monazite response to prograde metamorphism in the Reynolds Range, central Australia. Contrib. to Mineral. Petrol. 140, 458–468. https://doi.org/10.1007/PL00007673

Scaillet, B., Holtz, F., Pichavant, M., Schmidt, M., 1996. Viscosity of Himalayan leucogranites: Implications for mechanisms of granitic magma ascent. J. Geophys. Res. Solid Earth 101, 27691–27699. https://doi.org/10.1029/96JB01631

Schelling, D., 1992. The tectonostratigraphy and structure of the eastern Nepal Himalaya. Tectonics 11, 925–943. https://doi.org/10.1029/92TC00213

Searle, M.P., Cottle, J.M., Streule, M.J., Waters, D.J., 2009. Crustal melt granites and migmatites along the Himalaya: Melt source, segregation, transport and granite emplacement mechanisms. Earth and Environmental Science Transactions of the Royal Society of Edinburgh, 100(1-2), 219-233.

Searle, M.P., Phillips, R.J., 2009. Comment on: "Does the Karakoram fault interrupt mid-crustal channel flow in the western Himalaya?" by Mary L. Leech, Earth and Planetary Science Letters 276 (2008) 314-322. Earth Planet. Sci. Lett. 286, 589–591. https://doi.org/10.1016/j.epsl.2009.05.036

Seydoux-Guillaume, A.M., Paquette, J.L., Wiedenbeck, M., Montel, J.M., Heinrich, W., 2002. Experimental resetting of the U-Th-Pb systems in monazite. Chem. Geol. 191, 165–181. https://doi.org/10.1016/S0009-2541(02)00155-9

Stepanov, A.S., Hermann, J., Rubatto, D., Rapp, R.P., 2012. Experimental study of monazite/melt partitioning with implications for the REE, Th and U geochemistry of crustal rocks. Chem. Geol. 300–301, 200–22

Viskupic, K., Hodges, K. V, Bowring, S.A., 2005. Timescales of melt generation and the thermal evolution of the Himalayan metamorphic core, Everest region, eastern Nepal. Contrib. to Mineral. Petrol. 149, 1–21. https://doi.org/10.1007/s00410-004-0628-5

Viskupic, K., Hodges, K. V., 2001. Monazite–xenotime thermochronometry: methodology and an example from the Nepalese Himalaya. Contrib. to Mineral. Petrol. 141, 233–247. https://doi.org/10.1007/s004100100239

Weinberg, R.F., 2016. Himalayan leucogranites and migmatites: nature, timing and duration of anatexis. J. Metamorph. Geol. 34, 821–843. https://doi.org/10.1111/jmg.12204

Williams, I.S., 2001. Response of detrital and zircon and monazite, and their U-Pb isotopic systems, to regional metamorphism and host-rock partial melting, Cooma Complex, Southeastern Australia. Aust. J. Earth Sci. 48, 557–580. https://doi.org/10.1046/j.1440-0952.2001.00883.x

Williams, M.L., Jercinovic, M.J., Hetherington, C.J., 2007. Microprobe Monazite Geochronology: Understanding Geologic Processes by Integrating Composition and Chronology. Annu. Rev. Earth Planet. Sci. 35, 137–175. https://doi.org/10.1146/annurev.earth.35.031306.140228

10. Figure Captions

Figure 1. Simplified geologic map of the Tama Kosi region east-central Nepal modified from Larson, (2012) showing sample locations and existing monazite geochronology data from Larson

et al., (2013) and Larson and Cottle (2014). Location of study area is shown in generalized map of Nepal (inset).

Figure 2. Representative field photographs showing transition from dyke and sill network feeding into main pluton (a); (b-c) cross cutting relationships between pegmatitic (TK111B), medium-coarse grained (TK122) and (d) restitic (TK116) phases of plutonic complex in the upper Tama Kosi valley. Parts a-c modified from Fig. 8 in Larson, (2012).

Figure 3. Plane polarized light (left column) and cross-polarized light (right column) photomicrographs of Tama Kosi samples. A) Cross-cutting pegmatitic phase (TK111B). B) Medium-coarse grained phase (TK122). C) Restitic phase of plutonic complex (TK116). Bt - biotite, Ms - muscovite, Qz - quartz, Pl - plagioclase, Kfs - K-feldspar.

Figure 4. A) Representative pseudocolored Cathodoluminescence (CL) images of zircon from TK111B. Black circles are locations of spot analyses. Labels are ^{207}Pb-corrected ^{206}Pb/^{238}U dates. B - F) Representative compositional maps of monazite and xenotime for TK122 and TK116. Black circles are locations of Laser Ablation spot analyses. Labels in B, D, E are ^{208}Pb/^{232}Th dates, labels in C and F are ^{206}Pb/^{238}U dates. Full image sets and LASS data available in Figure DR1 and Table DR1, respectively.

Figure 5. Tera-Wasserberg (A, B, F) and ^{208}Pb/^{232}Th vs. ^{206}Pb/^{238}U Concordia diagrams (C, D, E) for zircon, xenotime and monazite from specimens TK111B, TK122 and TK116. Plots and

weighted mean dates were generated using a modified version of Redux (Bowring et al. (2011). Refer to Table DR1 for full dataset.

Figure 6. Summary age plot of U-Th/Pb zircon, monazite and xenotime dates for pegmatitic (TK111B), medium-coarse grained (TK122) and restitic (TK116) phases of plutonic complex in the upper Tama Kosi valley. 'Δ age' refers to the median age gap in Ma, the numerator after 'Δ age' is the difference between mean dates on either side of the gap, while the denominator is the minimum difference in dates, incorporating the uncertainties in both dates. Refer to Table DR1 for full dataset.

Figure 7. Monazite, xenotime and zircon trace element geochemistry plots for TK111B. Eu/Eu* is the europium anomaly calculated as '[Eu]/sqrt([Sm]*[Gd]), using concentrations normalized to chondrite. Th/U, Sm/La and Gd/Yb are elemental ratios. Whole rock (w.r.) values are provided for comparison. The shaded grey 'min. age gap' region is the 'age gap' identified in Fig. 6. Refer to Table DR1 for full dataset.

Figure 8. Monazite and xenotime trace element geochemistry plots for TK116 and TK122. Eu/Eu* is the europium anomaly calculated as [Eu]/sqrt([Sm]*[Gd]), using concentrations normalized to chondrite. Th/U, Sm/La and Gd/Yb are elemental ratios. For clarity, fields encompassing the entire range in values are presented for TK122 Sm/La and Gd/Yb. The shaded grey 'min. age gap' region is the 'age gap' identified in Fig. 6. Refer to Table DR1 for full dataset.

Figure 9. Yttrium equilibrium partition co-efficients (K_D) through time for TK111B and TK116 zircon (zrn), monazite (mnz) and xenotime (xnt). K_D values were computed by averaging trace element concentrations over 1 m.y. time intervals. Plots of other elements and element ratios (not shown) display similar trends. Refer to Table DR1 for full dataset.

Figure 10. Ti-in-zircon (Ferry and Watson, 2007) and Y-in monazite (Gratz and Heinrich, 1997) temperatures for TK111B and TK116 through time. TK111B whole rock apparent zircon-saturation (T_{Zr}) and monazite-saturation (T_{mnz}) temperatures are provided for comparison. The shaded grey 'min. age gap' region is the 'age gap' identified in Fig. 6. Refer to Table DR1 for full dataset.

Figure 11. Model temperature constraints for pegmatitic (TK111B) and medium-coarse grained (TK122) phases calculated using the measured bulk rock concentrations of Zr and LREE along with solubility expressions for (a) zircon (Boehnke et al., 2013) and (b) monazite (Stepanov et al., 2012). The vertical dashed lines are the bulk rock Zr and LREE concentrations measured by LA-ICP-MS. The intersection between the dashed line and the solid curves represents the temperature where zircon (a) and monazite (b) are expected to start crystallizing out of the melt due to Zr and LREE saturation with respect to these minerals. All calculations are done assuming a pressure of 4 kbar. Refer to Table DR 2 for full geochemical dataset.

Figure 12. Schematic history of leuogranite formation in the upper Tama Kosi region of Nepal. A) Accessory phase crystallization occurs in the future source region of TK111B under near isothermal conditions of 650 - 700C from ~28 - 21 Ma. B) At ~21 Ma, leucogranite generation

(TK122) is emplaced, accompanied by water influx and an increase in temperature which leads to a hiatus in accessory phase crystallization in the source of TK111B. C) Water influx and continued high temperature results in melt extraction and crystallization of pegmatite phase, TK111B at 19.4 - 18.6 Ma.

Figure DR 1: Part A) Pseudocolored Cathodoluminescence (CL) images of zircon from TK111B. Black circles are locations of spot analyses. Labels refer to analysis number in Table DR 1. **B - D)** WDS x-ray compositional maps of monazite from TK122 **(part B),** monazite from TK111B **part C)** and xenotime monazite from TK111B (**part D**). Black circles are locations of Laser Ablation spot analyses, label numbers refer to analysis number in Table DR 1. Full LASS data available in Table DR1.

Table DR 1: U-Th/Pb and Trace element concentration data for zircon, monazite and xenotime from samples from the Tama Kosi Valley, Nepal.

Table DR 2: Table 2: Major and trace element concentrations of samples from the Tama Kosi Valley, Nepal.

Highlights:

- Protracted crystallization of accessory minerals in source region of pegmatite dikes

- Majority of accessory mineral domains in pegmatite pre-dates igneous history

- Pause in accessory crystallization caused by heat and water influx from main granite

- Petrochronlogy is key to understanding protracted history of anatexis in the Himalaya

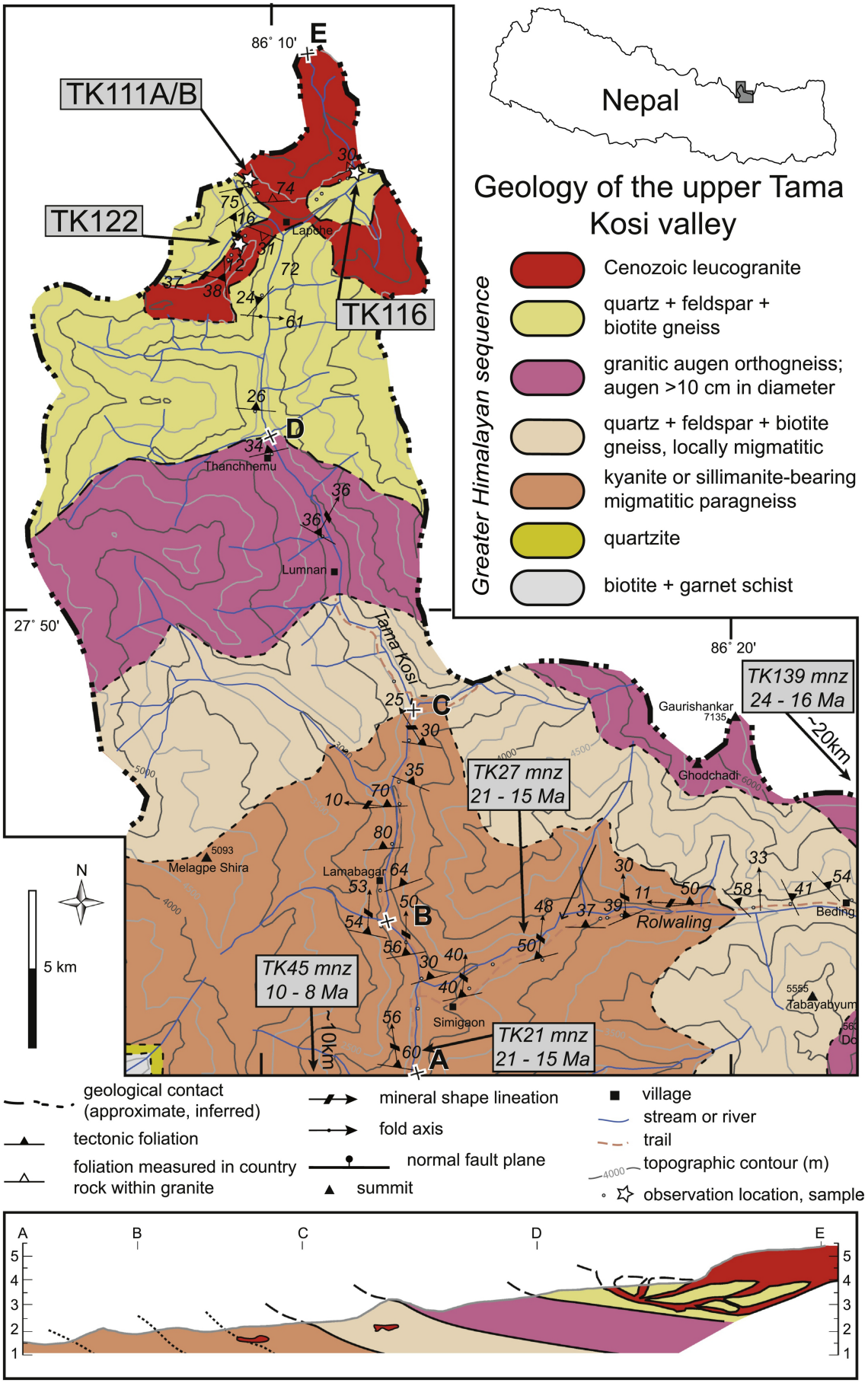
Nepal
Geology of the upper Tama Kosi valley
Greater Himalayan sequence
Cenozoic leucogranite
quartz + feldspar + biotite gneiss
granitic augen orthogneiss; augen >10 cm in diameter
quartz + feldspar + biotite gneiss, locally migmatitic
kyanite or sillimanite-bearing migmatitic paragneiss
quartzite
biotite + garnet schist
TK111A/B
TK122
TK116
TK139 mnz 24 - 16 Ma
TK27 mnz 21 - 15 Ma
TK45 mnz 10 - 8 Ma
TK21 mnz 21 - 15 Ma
~20km
10km
86° 10'
86° 20'
27° 50'
Tama Kosi
Lapche
Thanchhemu
Lumnan
Gaurishankar 7135
Ghodchadi
Melagpe Shira 5093
Lamabagar
Rolwaling
Beding
Tabayabyum 5555
Simigaon
5 km
N
geological contact (approximate, inferred)
tectonic foliation
foliation measured in country rock within granite
mineral shape lineation
fold axis
normal fault plane
summit
village
stream or river
trail
topographic contour (m)
observation location, sample
A
B
C
D
E

Figure 1

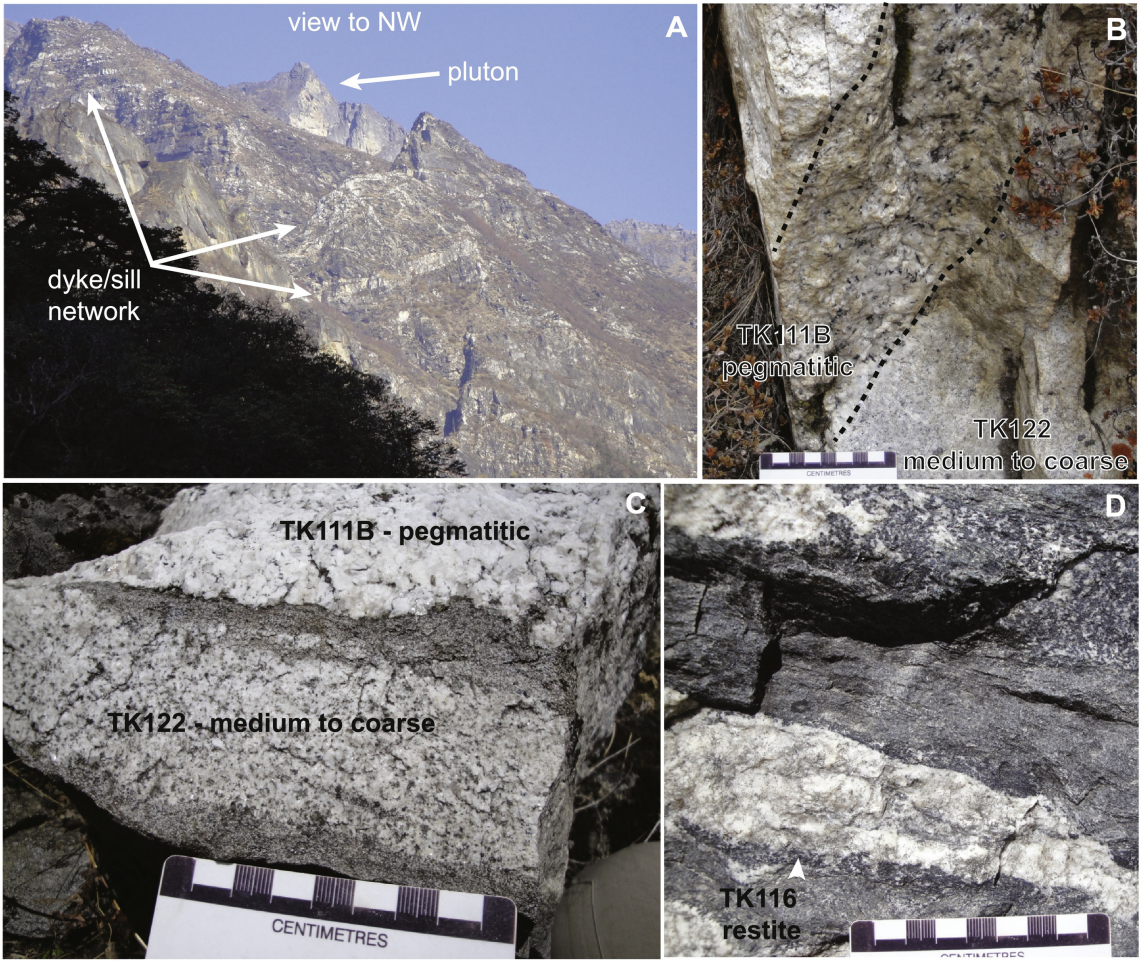
A
view to NW
pluton
dyke/sill
network
B
TK111B
pegmatitic
TK122
medium to coarse
C
TK111B - pegmatitic
TK122 - medium to coarse
CENTIMETRES
D
TK116
restite

Figure 2

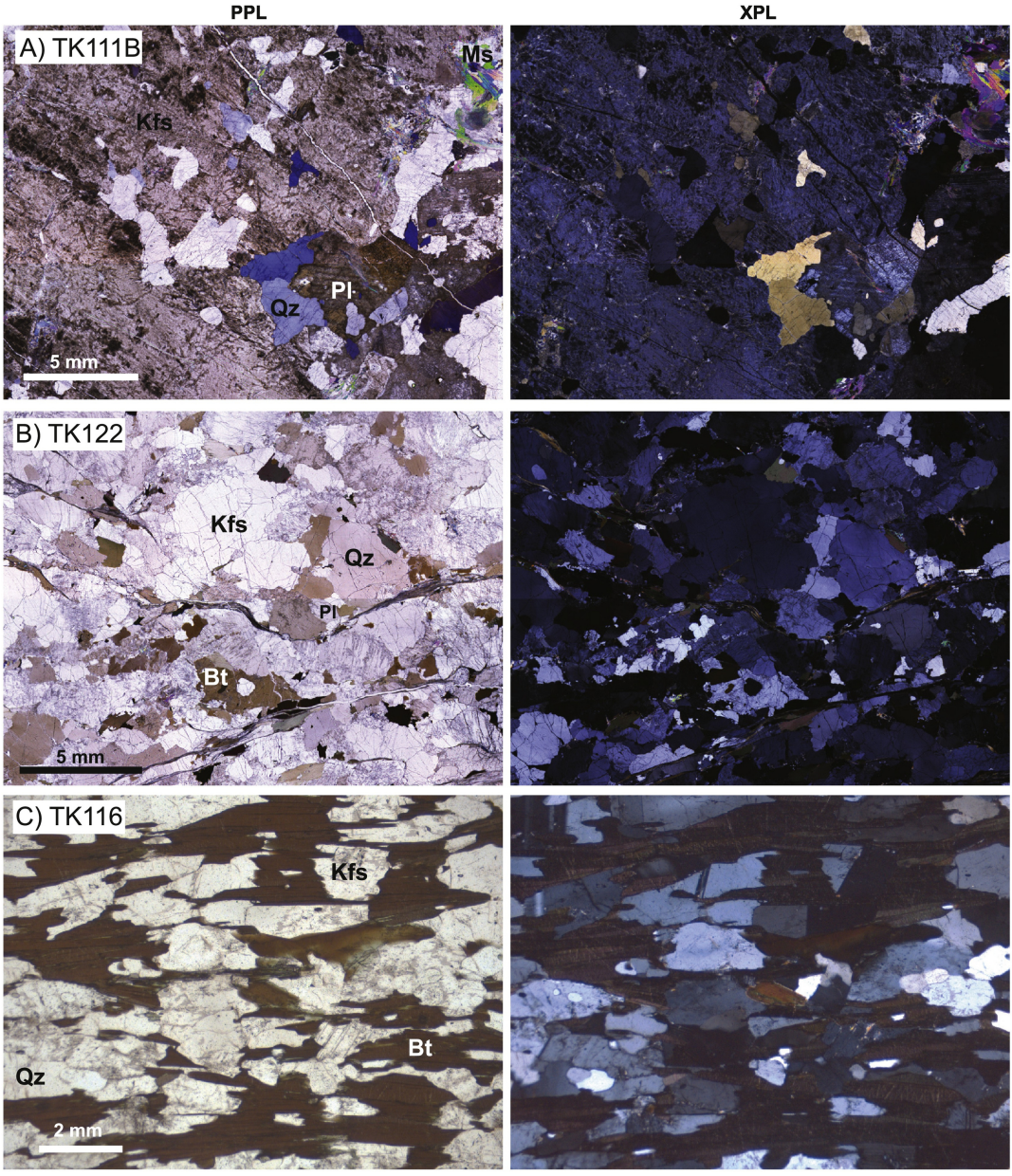
PPL
XPL
A) TK111B
Ms
Kfs
Qz
Pl
5 mm
B) TK122
Kfs
Qz
Pl
Bt
5 mm
C) TK116
Kfs
Bt
Qz
2 mm

Figure 3

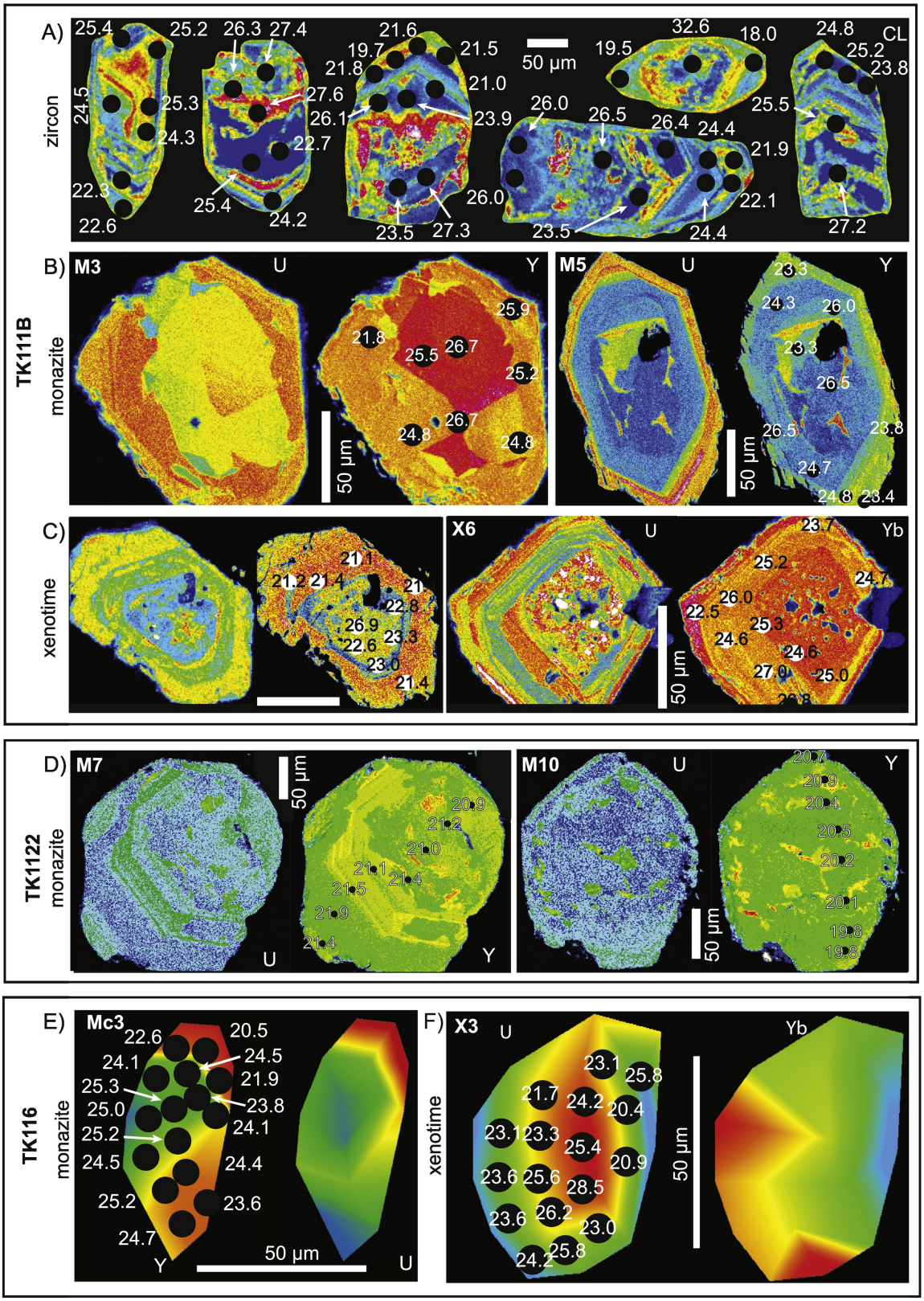
A)
zircon
CL
50 µm
B)
TK111B
monazite
M3
U
Y
M5
50 µm
C)
xenotime
X6
U
Yb
50 µm
D)
TK1122
monazite
M7
U
Y
50 µm
M10
U
Y
50 µm
E)
TK116
monazite
Mc3
Y
50 µm
U
F)
xenotime
X3
U
Yb
50 µm
Low
CL response /
relative concentration
High

Figure 4

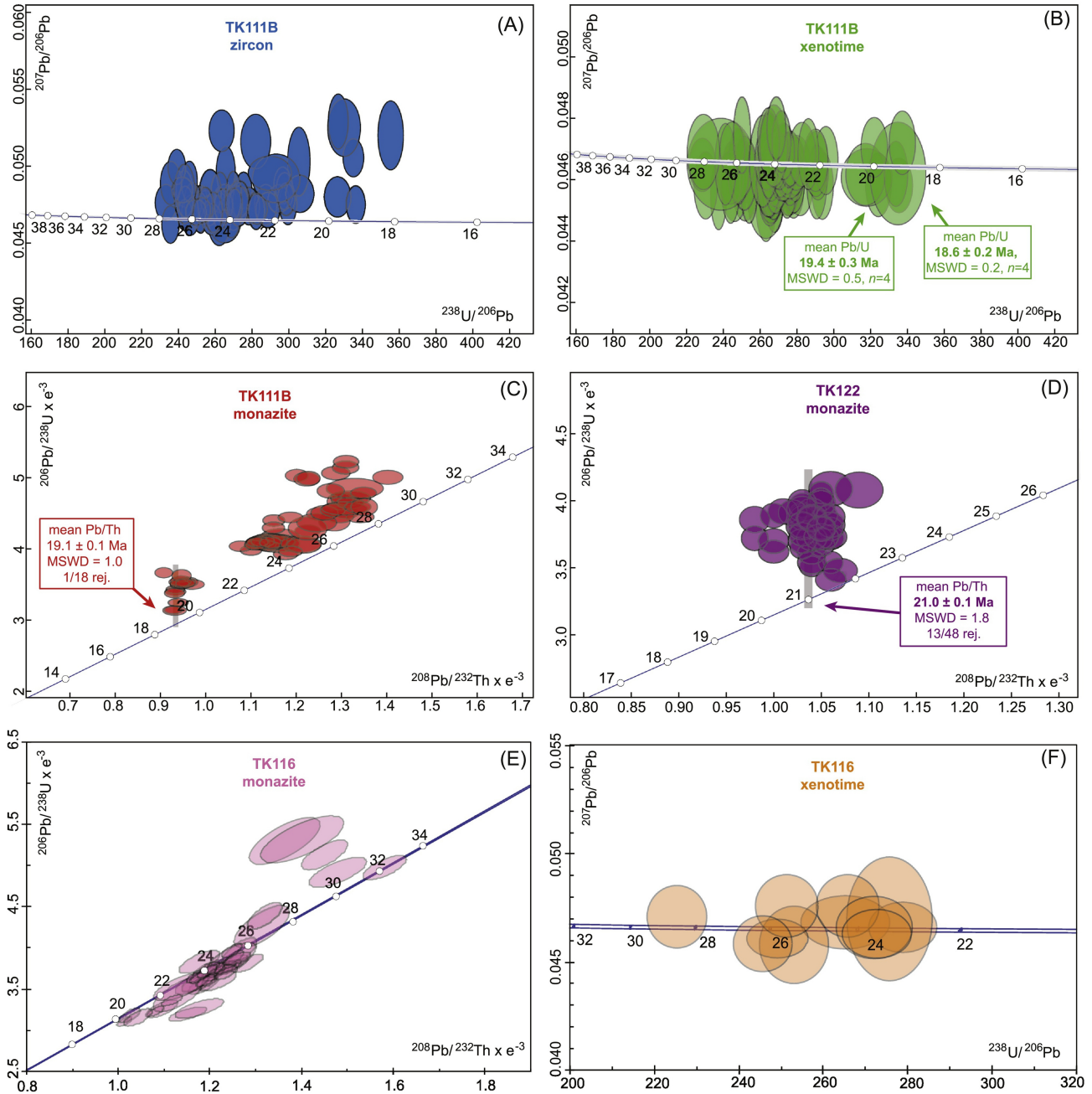
(A)
TK111B
zircon
$^{207}Pb/^{206}Pb$
$^{238}U/^{206}Pb$
(B)
TK111B
xenotime
mean Pb/U
19.4 ± 0.3 Ma
MSWD = 0.5, n=4
mean Pb/U
18.6 ± 0.2 Ma,
MSWD = 0.2, n=4
(C)
TK111B
monazite
mean Pb/Th
19.1 ± 0.1 Ma
MSWD = 1.0
1/18 rej.
$^{206}Pb/^{238}U$ x e^{-3}
$^{208}Pb/^{232}Th$ x e^{-3}
(D)
TK122
monazite
mean Pb/Th
21.0 ± 0.1 Ma
MSWD = 1.8
13/48 rej.
(E)
TK116
monazite
(F)
TK116
xenotime

Figure 5

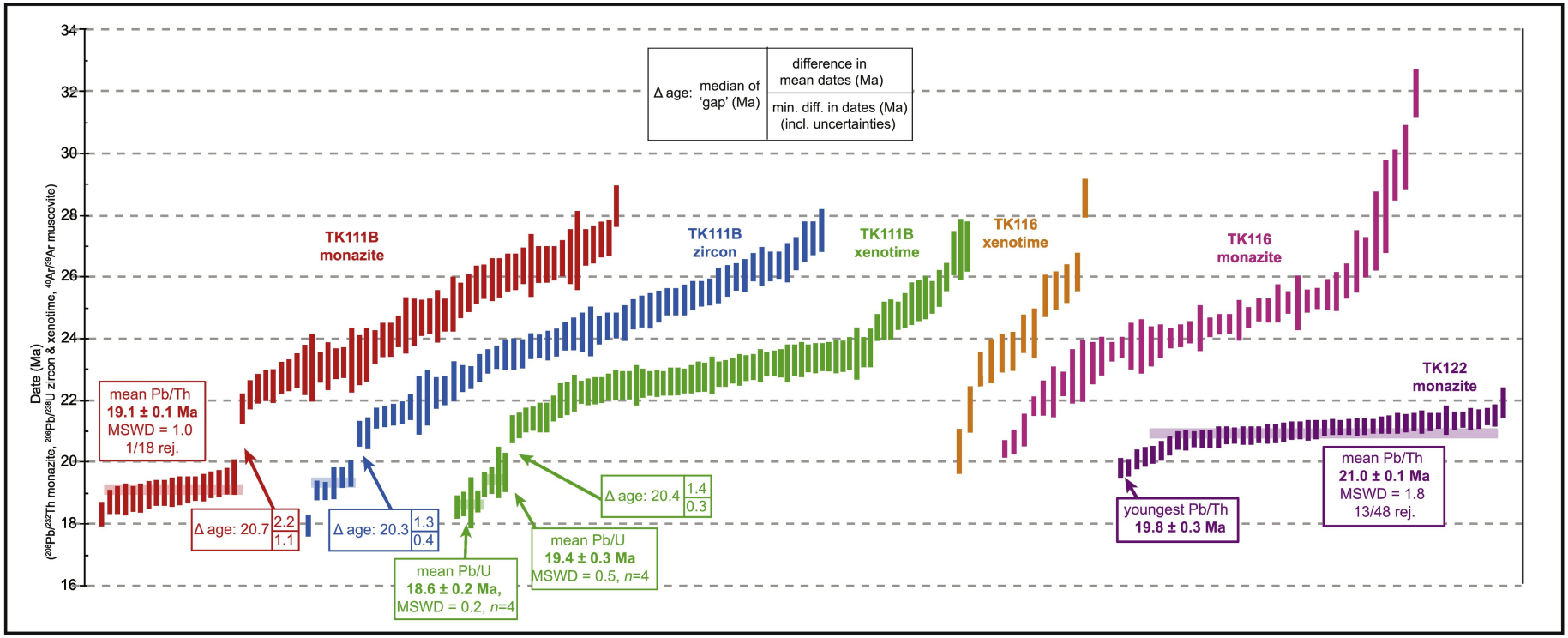
Δ age: median of 'gap' (Ma)
difference in mean dates (Ma)
min. diff. in dates (Ma) (incl. uncertainties)
Date (Ma)
(208Pb/232Th monazite, 208Pb/238U zircon & xenotime, 40Ar/39Ar muscovite)
34
32
30
28
26
24
22
20
18
16
TK111B monazite
TK111B zircon
TK111B xenotime
TK116 xenotime
TK116 monazite
TK122 monazite
mean Pb/Th
19.1 ± 0.1 Ma
MSWD = 1.0
1/18 rej.
Δ age: 20.7
2.2
1.1
Δ age: 20.3
1.3
0.4
mean Pb/U
18.6 ± 0.2 Ma,
MSWD = 0.2, n=4
mean Pb/U
19.4 ± 0.3 Ma
MSWD = 0.5, n=4
Δ age: 20.4
1.4
0.3
youngest Pb/Th
19.8 ± 0.3 Ma
mean Pb/Th
21.0 ± 0.1 Ma
MSWD = 1.8
13/48 rej.

Figure 6

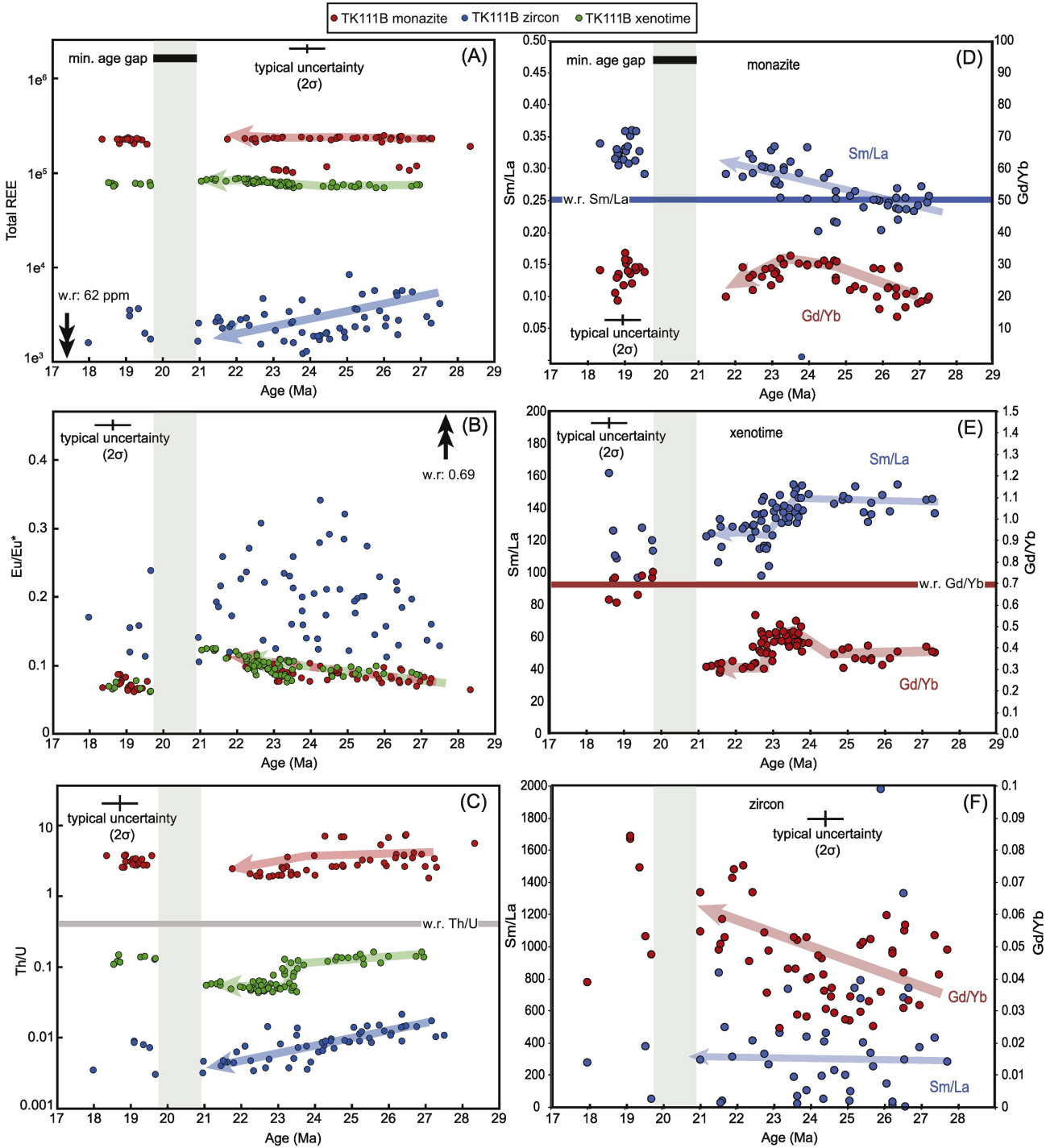
TK111B monazite
TK111B zircon
TK111B xenotime
(A)
min. age gap
typical uncertainty (2σ)
Total REE
w.r: 62 ppm
Age (Ma)
(D)
monazite
Sm/La
Gd/Yb
w.r. Sm/La
Gd/Yb
(B)
Eu/Eu*
w.r: 0.69
(E)
xenotime
w.r. Gd/Yb
(C)
Th/U
w.r. Th/U
(F)
zircon

Figure 7

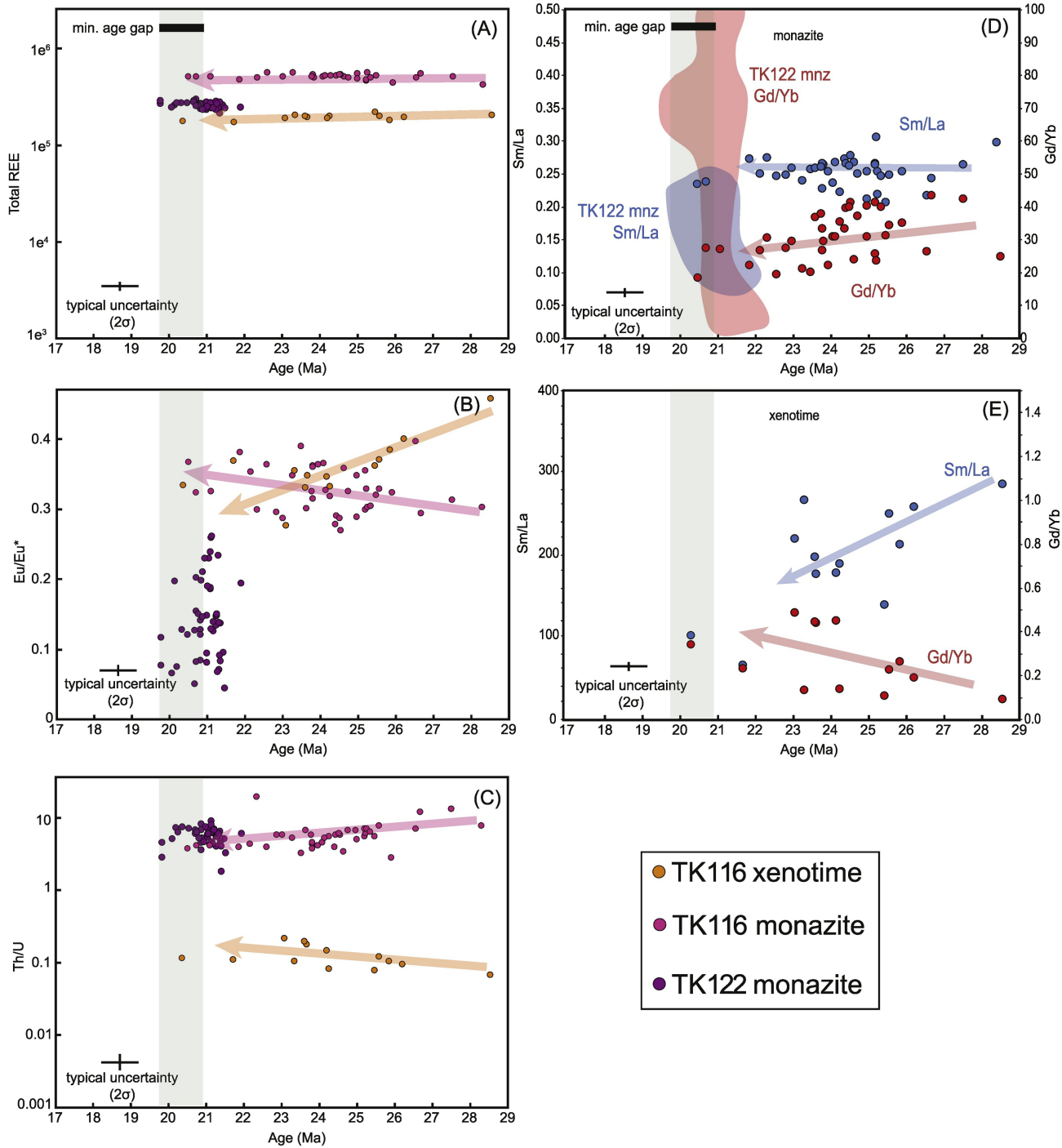
(A)
min. age gap
Total REE
typical uncertainty (2σ)
Age (Ma)
(D)
monazite
TK122 mnz Gd/Yb
Sm/La
TK122 mnz Sm/La
Gd/Yb
Sm/La
Gd/Yb
(B)
Eu/Eu*
(E)
xenotime
(C)
Th/U
TK116 xenotime
TK116 monazite
TK122 monazite

Figure 8

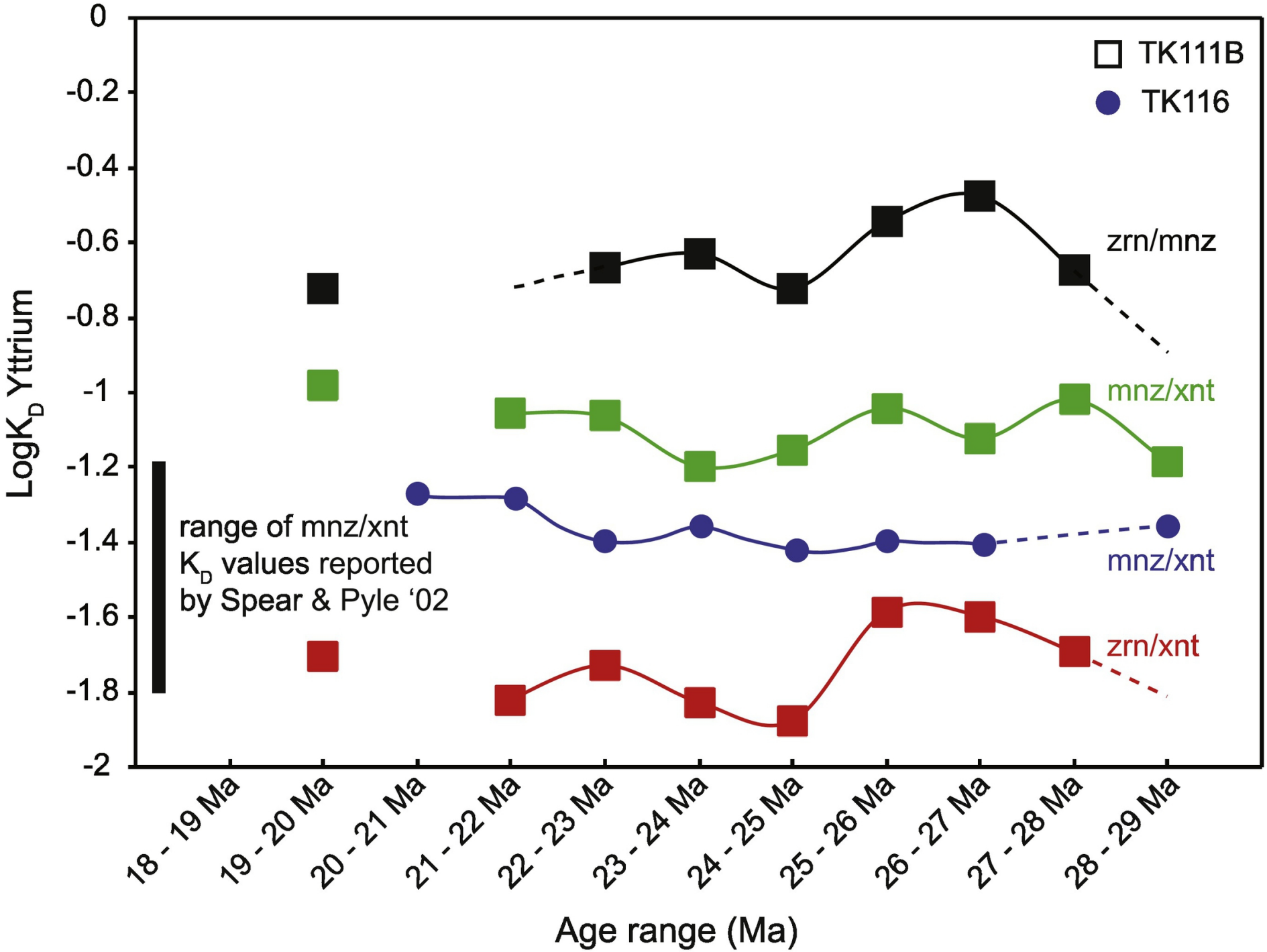
TK111B
TK116
zrn/mnz
mnz/xnt
mnz/xnt
zrn/xnt
range of mnz/xnt
K_D values reported
by Spear & Pyle '02
LogK_D Yttrium
0
-0.2
-0.4
-0.6
-0.8
-1
-1.2
-1.4
-1.6
-1.8
-2
18 - 19 Ma
19 - 20 Ma
20 - 21 Ma
21 - 22 Ma
22 - 23 Ma
23 - 24 Ma
24 - 25 Ma
25 - 26 Ma
26 - 27 Ma
27 - 28 Ma
28 - 29 Ma
Age range (Ma)

Figure 9

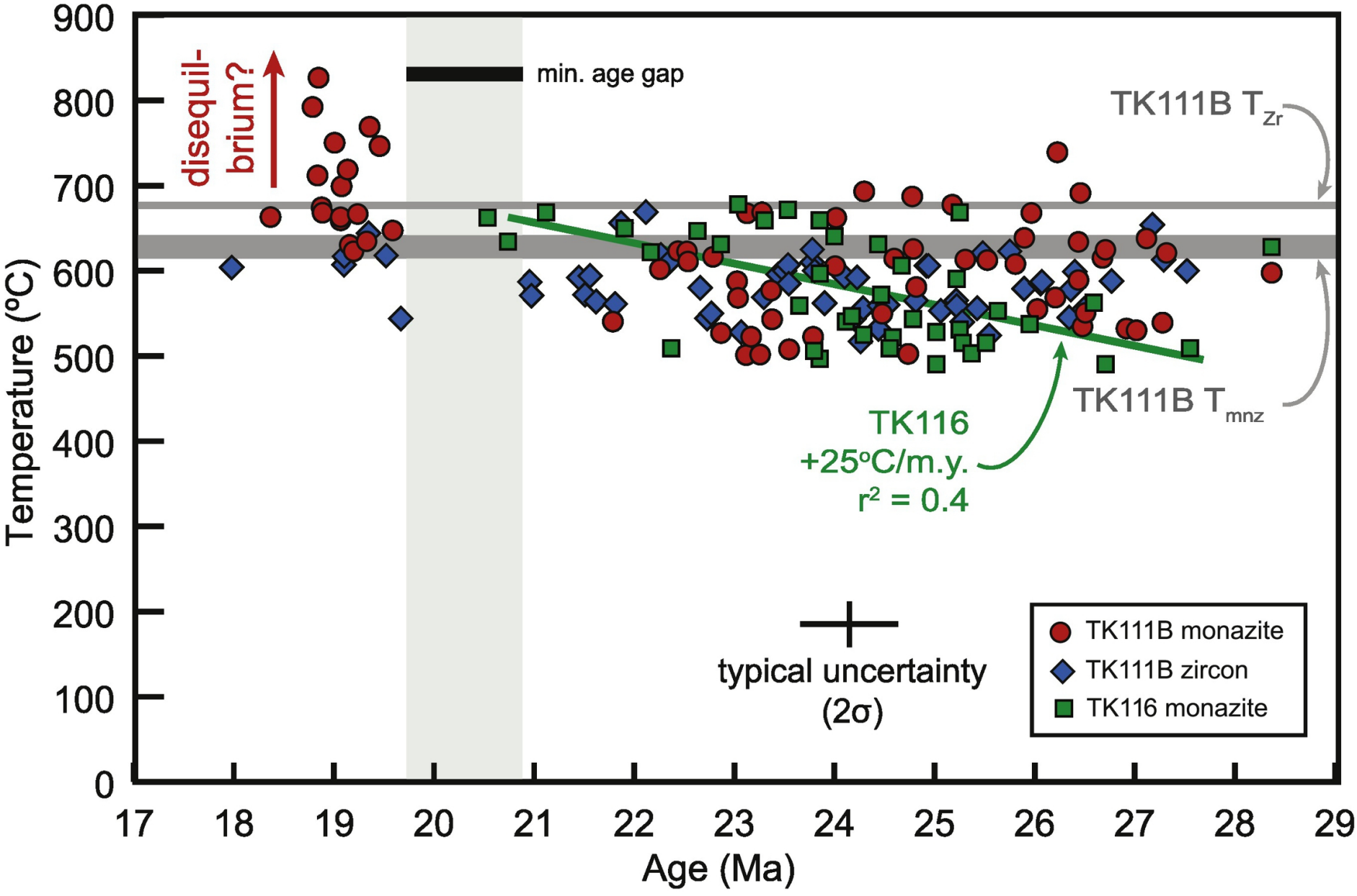
900
800
700
600
500
400
300
200
100
0
Temperature (°C)
17
18
19
20
21
22
23
24
25
26
27
28
29
Age (Ma)
disequil-
brium?
min. age gap
TK111B T_{Zr}
TK111B T_{mnz}
TK116
+25°C/m.y.
r^2 = 0.4
typical uncertainty
(2σ)
TK111B monazite
TK111B zircon
TK116 monazite

Figure 10

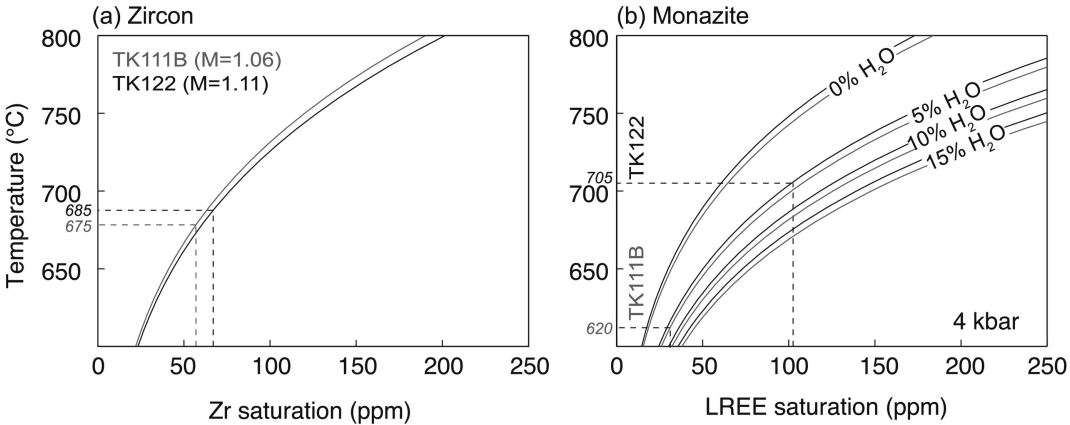
(a) Zircon
TK111B (M=1.06)
TK122 (M=1.11)
Temperature (°C)
800
750
700
650
685
675
0
50
100
150
200
250
Zr saturation (ppm)
(b) Monazite
0% H2O
5% H2O
10% H2O
15% H2O
TK122
TK111B
705
620
4 kbar
LREE saturation (ppm)

Figure 11

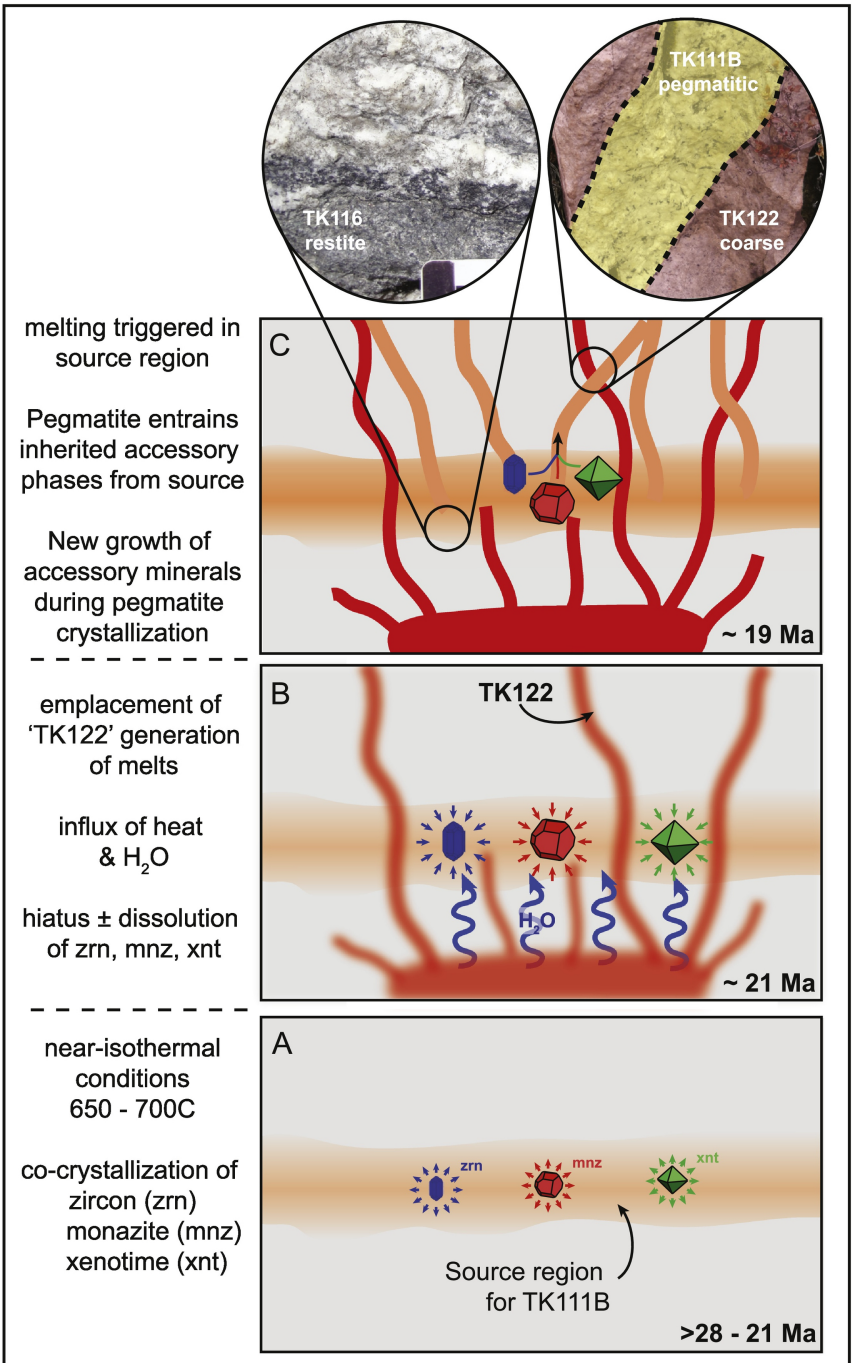
TK116
restite
TK111B
pegmatitic
TK122
coarse
melting triggered in source region
Pegmatite entrains inherited accessory phases from source
New growth of accessory minerals during pegmatite crystallization
C
~ 19 Ma
emplacement of 'TK122' generation of melts
influx of heat & H2O
hiatus ± dissolution of zrn, mnz, xnt
B
TK122
H2O
~ 21 Ma
near-isothermal conditions 650 - 700C
co-crystallization of zircon (zrn) monazite (mnz) xenotime (xnt)
A
zrn
mnz
xnt
Source region for TK111B
>28 - 21 Ma

Figure 12

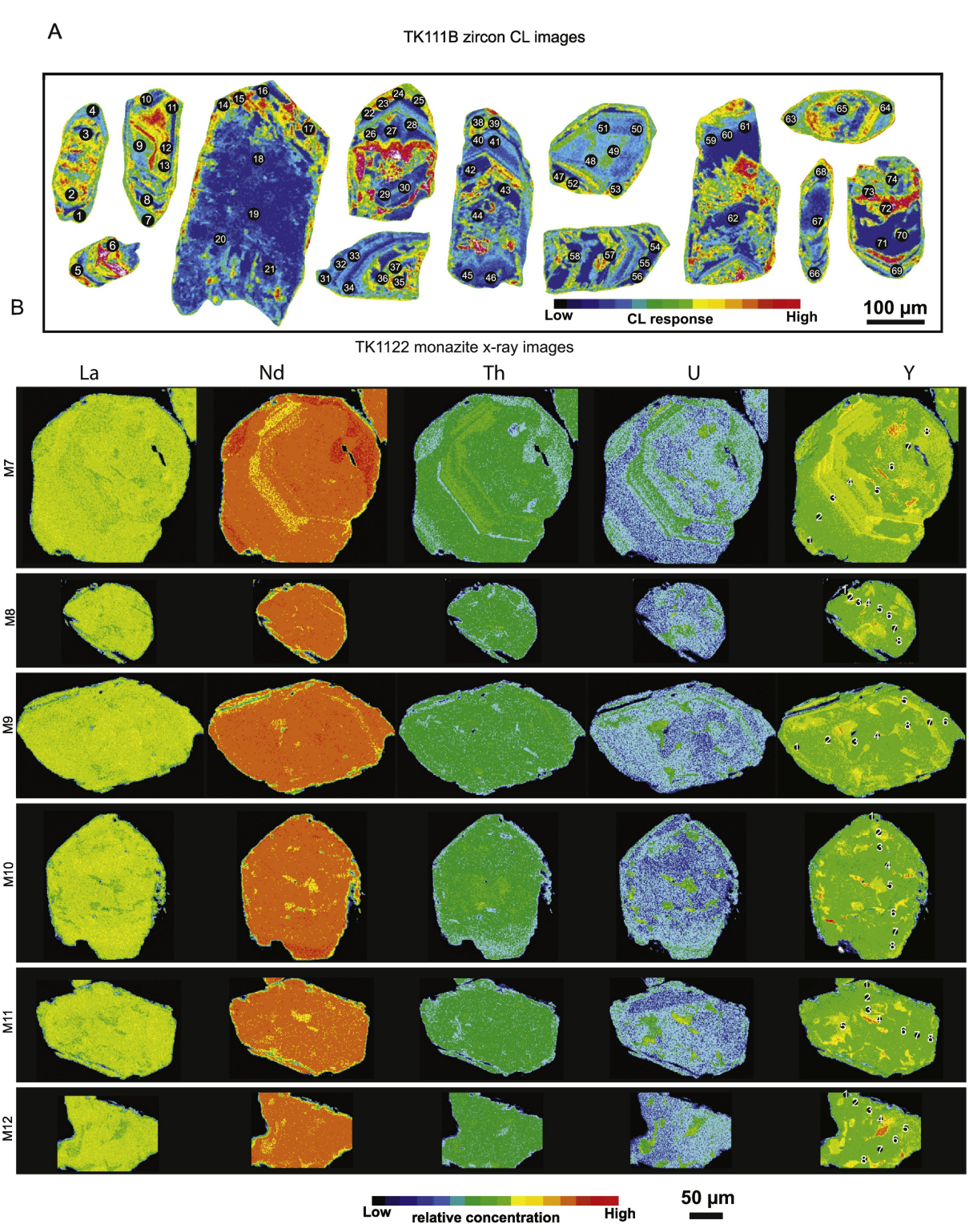
A
TK111B zircon CL images
B
Low
CL response
High
100 µm
TK1122 monazite x-ray images
La
Nd
Th
U
Y
M7
M8
M9
M10
M11
M12
Low
relative concentration
High
50 µm

Figure 13ab

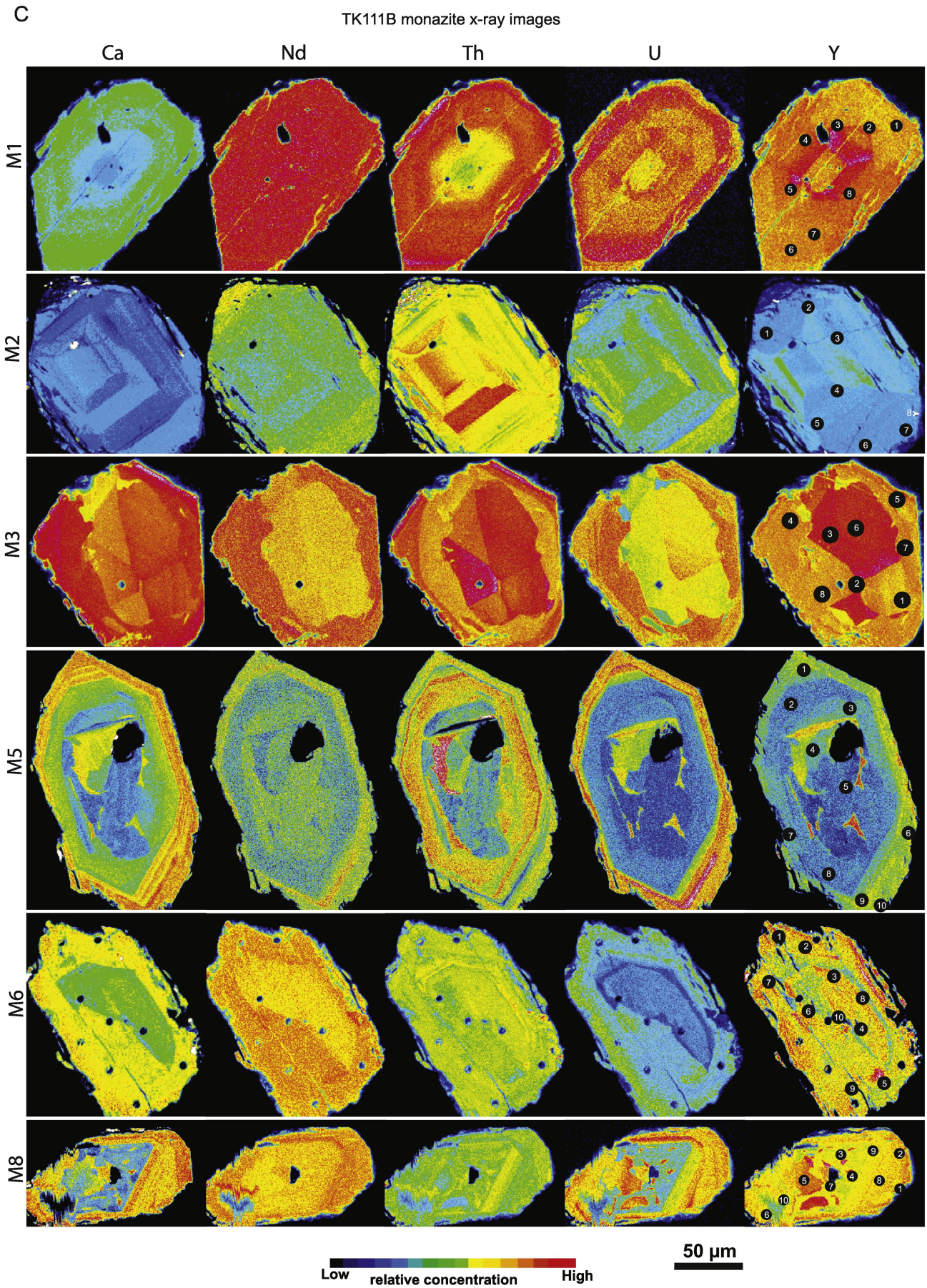
C
TK111B monazite x-ray images
Ca
Nd
Th
U
Y
M1
M2
M3
M5
M6
M8
Low
relative concentration
High
50 µm

Figure 13c

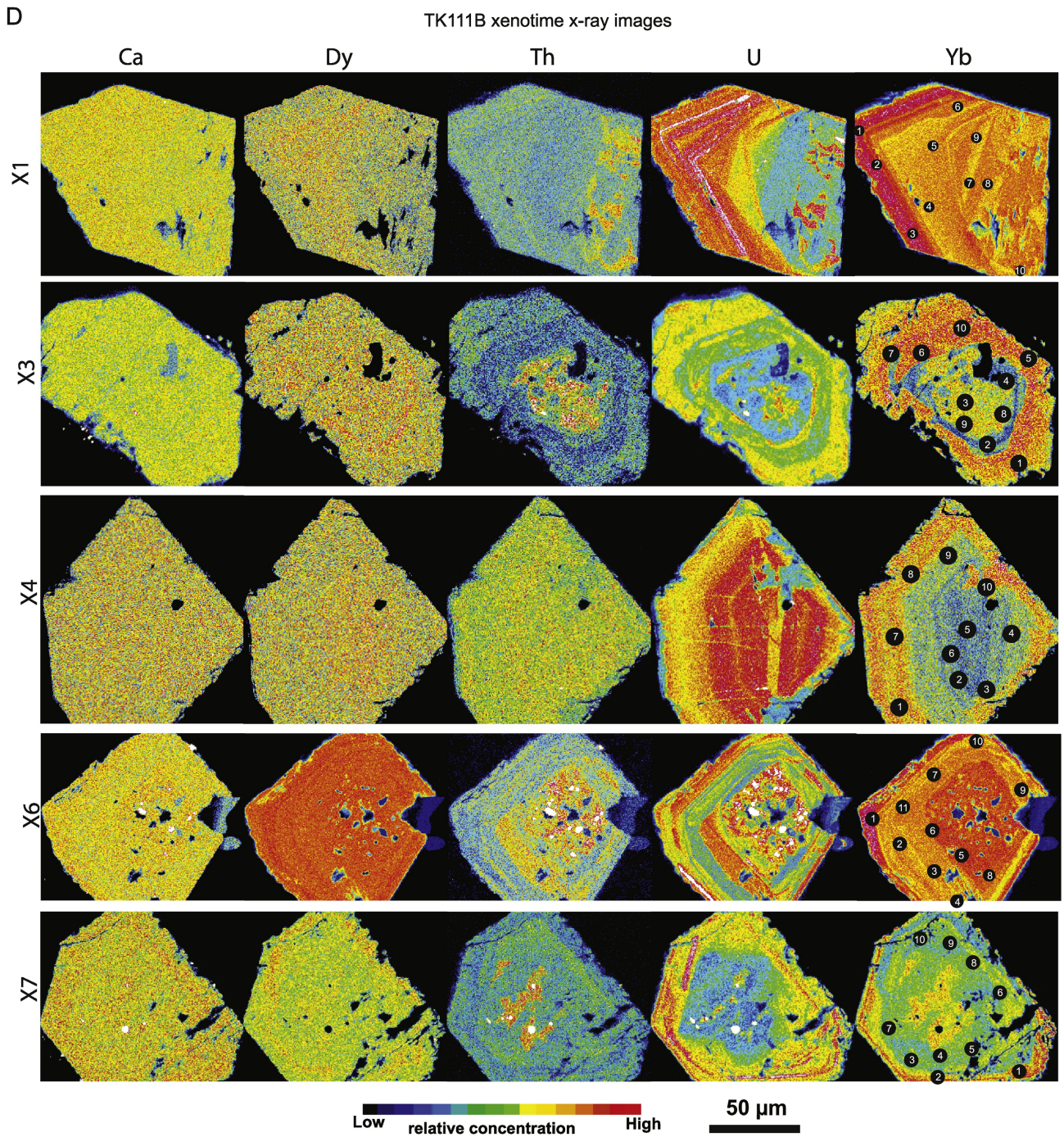
D
TK111B xenotime x-ray images
Ca
Dy
Th
U
Yb
X1
X3
X4
X6
X7
Low
relative concentration
High
50 µm

Figure 13d